The Astrophysical Journal, 952:109 (22pp), 2023 August 1 https://doi.org/10.3847/1538-4357/acc8d3

The Spatial Clustering of ROSAT All-Sky Survey Active Galactic Nuclei. V. The Evolution of Broad-line AGN Clustering Properties in the Last 6 Gyr

Mirko Krumpe[1], Takamitsu Miyaji[2,1,11], Antonis Georgakakis[3,4], Andreas Schulze[5,6], Alison L. Coil[7], Tom Dwelly[4], Damien Coffey[4], Johan Comparat[4], Héctor Aceves[2], Mara Salvato[4], Andrea Merloni[4], Claudia Maraston[8], Kirpal Nandra[4], Joel R. Brownstein[9], and Donald P. Schneider[10]
SDSS-IV Team and SPIDERS Team

[1] Leibniz-Institut für Astrophysik Potsdam (AIP), An der Sternwarte 16, D-14482 Potsdam, Germany; mkrumpe@aip.de
[2] Universidad Nacional Autónoma de México (UNAM), Instituto de Astronomía, AP 106, Ensenada 22860, BC, México
[3] IAASARS, National Observatory of Athens, GR-15236 Penteli, Greece
[4] Max-Planck-Institut für extraterrestrische Physik, Gießenbachstraße 1, D-85748 Garching, Germany
[5] National Astronomical Observatory of Japan, Mitaka, Tokyo 181-8588, Japan
[6] OmagaLambdaTec, Lichtenbergstraße 8, D-85748 Garching, Germany
[7] University of California, San Diego, Center for Astrophysics and Space Sciences, 9500 Gilman Drive, La Jolla, CA 92093-0424, USA
[8] Institute of Cosmology and Gravitation, Burnaby Road, Portsmouth, PO1 3FX, UK
[9] Department of Physics and Astronomy, University of Utah, 115 S. 1400 E., Salt Lake City, UT 84112, USA
[10] Department of Astronomy and Astrophysics, The Pennsylvania State University, University Park, PA 16802, USA
Received 2022 December 21; revised 2023 March 20; accepted 2023 March 28; published 2023 July 21

Abstract

This is the fifth paper in a series of investigations of the clustering properties of luminous, broad-emission-line active galactic nuclei (AGNs) identified in the ROSAT All-Sky Survey (RASS) and Sloan Digital Sky Survey (SDSS). In this work we measure the cross-correlation function (CCF) between RASS/SDSS Data Release 14 AGNs with the SDSS CMASS galaxy sample at $0.44 < z < 0.64$. We apply halo occupation distribution (HOD) modeling to the CCF along with the autocorrelation function of the CMASS galaxies. We find that X-ray-selected and optically selected AGNs at $0.44 < z < 0.64$ reside in statistically identical halos with a typical dark matter halo (DMH) mass of $M_{\rm DMH}^{\rm typ,AGN} \sim 10^{12.7}\,h^{-1}\,M_{\odot}$. The acceptable HOD parameter space for these two broad-line AGN samples have only statistically marginal differences caused by small deviations of the CCFs in the one-halo-dominated regime on small scales. In contrast to optically selected AGNs, the X-ray AGN sample may contain a larger population of satellites at $M_{\rm DMH} \sim 10^{13}\,h^{-1}\,M_{\odot}$. We compare our measurements in this work with our earlier studies at lower independent redshift ranges, spanning a lookback time of 6 Gyr. The comparison over this wider redshift range of $0.07 < z < 0.64$ reveals (i) no significant difference between the typical DMH masses of X-ray-selected and optically selected AGNs, (ii) weak positive clustering dependencies of $M_{\rm DMH}^{\rm typ,AGN}$ with $L_{\rm X}$ and $M_{\rm BH}$, (iii) no significant dependence of $M_{\rm DMH}^{\rm typ,AGN}$ on Eddington ratio, and (iv) the same DMH masses host more-massive accreting black holes at high redshift than at low redshifts.

Unified Astronomy Thesaurus concepts: Active galaxies (17); Large-scale structure of the universe (902); X-ray active galactic nuclei (2035)

1. Introduction

According to the consensus cosmological model, primordial density fluctuations grow and collapse into gravitationally bound regions called dark matter halos (DMHs). Their gravitational interaction with baryonic matter leads to the formation of galaxies within these DMHs (e.g., White & Frenk 1991). Processes that are still poorly understood can lead to a flow of matter onto the supermassive black holes (SMBHs) at the centers of the galaxies. Such an object would be observed as an active galactic nucleus (AGN) until the mass flow onto the SMBH stops. The physical processes leading to the formation and evolution of galaxies (and their AGN phases) are closely connected with their host DMHs. However, these DMHs cannot be observed directly.

One approach to determine the properties of the DMHs is to measure the clustering of extragalactic objects hosted by these DMHs. This is commonly done by measuring the two-point correlation function (e.g., Peebles 1980). Since AGNs can be detected at a variety of wavelength ranges in sufficiently large samples, observational and theoretical studies have investigated the relationship between AGNs and their DMHs. AGN clustering measurements (see review by Krumpe et al. 2014) reveal important physical results on AGN/galaxy coevolution, typical DMHs, and the full distribution of DMH masses hosting AGNs (e.g., Porciani et al. 2004; Gilli et al. 2005, 2009; Yang et al. 2006; Coil et al. 2009; Ross et al. 2009; Krumpe et al. 2010, 2018; Cappelluti et al. 2010; Miyaji et al. 2011; Allevato et al. 2011; Mountrichas & Georgakakis 2012; Koutoulidis et al. 2013; Melnyk et al. 2018; Powell et al. 2018, 2020; Plionis et al. 2018; Mountrichas et al. 2019; Viitanen et al. 2019; Krishnan et al. 2020). Simulations and theoretical work (e.g., Springel 2005; Booth & Schaye 2010; Comparat et al. 2019; Georgakakis et al. 2019; Shankar et al. 2020) can use these observational constraints, as well as observed clustering dependences with AGN parameters, to improve models of AGN and galaxy evolution.

[11] On sabbatical leave from UNAM at AIP.

As AGN samples are substantially smaller than galaxy samples at low ($z \lesssim 0.7$) and moderate redshifts ($0.7 \lesssim z \lesssim 1.5$), the AGN autocorrelation function (ACF; measuring the distances between AGNs only) has a limited signal-to-noise ratio (S/N), particularly at small separations. To overcome this observational challenge, the AGN cross-correlation function (CCF) with a dense galaxy sample in the same volume can be used; Coil et al. (2009) demonstrate the potential of this approach. Due to the substantial increase in the number of AGN-galaxy pairs, the uncertainty in the clustering measurement is reduced compared to the measurement of the ACF in the same AGN sample. The AGN ACF can then be inferred from the AGN-galaxy CCF. Halo occupation distribution (HOD) modeling can then be used to interpret the observed clustering signal (e.g., Cooray & Sheth 2002; Rodríguez-Torres et al. 2017).

In Krumpe et al. (2010, hereafter Paper I), we use the CCF technique to measure the clustering between ROSAT All-Sky Survey (RASS) AGNs identified in the Sloan Digital Sky Survey (SDSS) and a large sample of SDSS luminous red galaxies (LRGs) at $0.16 < z < 0.36$. The samples are drawn from a series of SDSS data releases, starting with Data Release 4 (Adelman-McCarthy et al. 2006). The high S/N of the measurement allows us to split the sample into low and high X-ray luminosity subsamples. We find a weak X-ray luminosity dependence for luminous, broad-line AGNs in which higher-luminosity (median intrinsic $L_{0.1\text{–}2.4\,\mathrm{keV}} = 3.0 \times 10^{44}$ erg s^{-1}) AGNs cluster more strongly than their lower-luminosity (9.8×10^{43} erg s^{-1}) counterparts.

In the second paper of this series (Miyaji et al. 2011, hereafter Paper II), we develop a novel method of applying the HOD modeling technique directly to the measured CCF between RASS/SDSS AGNs and SDSS LRGs. We constrain the distribution of AGNs as a function of DMH mass instead of quoting only typical DMH masses. The major advantage of this method is that it does not use a phenomenological power-law fit, as is often done to derive typical DMHs. We find that models where the AGN fraction among satellite galaxies decreases with DMH mass beyond $M_{\mathrm{DMH}} \sim 10^{12}\ h^{-1}\ M_{\odot}$ are preferred for luminous, broad-line AGNs. This is in contrast to HOD modeling of galaxy samples (Zheng et al. 2009; Zehavi et al. 2011).

In the third paper (Krumpe et al. 2012, hereafter Paper III), we extend the cross-correlation measurements to lower and higher redshifts, covering a redshift range of $z = 0.07$–0.50 and apply the HOD modeling to all CCFs directly. We show that the weak X-ray luminosity dependence of broad-line AGN clustering is also found if radio-detected AGNs are excluded, and that optically and X-ray-selected AGN samples in SDSS show no significant difference in their clustering properties.

In the fourth paper (Krumpe et al. 2015, hereafter Paper IV), we explore the physical origin of the weak X-ray luminosity. We find that the clustering strength of luminous, broad-line AGNs depends on M_{BH} and not on L/L_{EDD}. Thus, more-massive SMBHs are hosted by more-massive DMHs than lower-mass SMBHs.

In this paper we extend the redshift range for our RASS/SDSS AGN clustering measurements further. We compute the CCF between AGN and SDSS CMASS galaxies in the redshift range $0.44 < z < 0.64$. We investigate the clustering dependencies for optically and X-ray-selected AGNs in this redshift range as well as for AGN parameters such as L_{X}, M_{i}, M_{BH}, L/L_{EDD}, and L_{Bol}. Combining these new measurements with the previous independent measurements at lower redshift allows us to constrain the evolution of the AGN clustering properties over a lookback time of 6 Gyr.

This paper is organized as follows. In Section 2 we describe the properties of the CMASS galaxy tracer set and the X-ray and optical AGN samples. Section 3 provides details on how we fit the Hα line profile in the optical SDSS AGN spectra, derive the M_{BH}, estimate L/L_{EDD}, and define our AGN subsamples. In Section 4 we briefly summarize the cross-correlation technique, how the AGN ACF is inferred from this, and how we derive the clustering parameters using HOD modeling. Section 5 provides the results of our clustering measurements. Our results are discussed in Section 6, and we present our conclusions in Section 7.

Throughout the paper, all distances are measured in comoving coordinates and given in units of h^{-1} Mpc, where $h = H_0/100$ km s^{-1} Mpc^{-1}, unless otherwise stated. We use a cosmology of $\Omega_{\mathrm{m}} = 0.3$, $\Omega_{\Lambda} = 0.7$, and $\sigma_8(z = 0) = 0.8$, which is consistent with the Wilkinson Microwave Anisotropy Probe Data Release 7 (DR7; Table 3 of Larson et al. 2011). The same cosmology is used in Papers I–IV. Luminosities and absolute magnitudes are calculated for $h = 0.7$. We use AB magnitudes throughout the paper. The symbol "log" represents a base-10 logarithm. All uncertainties represent 1σ (68.3%) confidence intervals unless otherwise stated.

2. Data

The data sets used in this study are drawn from the SDSS Data Releases 12 (DR12; Alam et al. 2015) and 14 (DR14; Abolfathi et al. 2018). The data were obtained as part of the SDSS-III (Eisenstein et al. 2011) Baryon Oscillation Spectroscopic Survey (BOSS; Dawson et al. 2013) using the BOSS spectrograph (Smee et al. 2013) on the 2.5 m SDSS telescope (Gunn et al. 2006). In the following subsections, we explain the sample selection of the CMASS (for "constant mass") SDSS sample (DR12), which serves as a tracer set of underlying dark matter density. We also give a description of the X-ray-selected RASS/SDSS AGN (DR14) and optical SDSS AGN (DR14) samples.

2.1. SDSS CMASS Galaxy Sample

Similar to LRGs, the target selection of CMASS galaxies is based on colors from the imaging survey of SDSS. However, the selection cuts for the CMASS sample are fainter and bluer than those of the LRG sample. The CMASS sample is approximately stellar mass limited and covers a redshift range of $z \sim 0.43$–0.7. For more details, see, e.g., Dawson et al. (2013), Guo et al. (2013), Maraston et al. (2013), and Ross et al. (2017).

The original spectroscopic CMASS sample can be downloaded online. For this work, we focus only on data from the SDSS North Cap ($100 \leqslant$ R. A. $\leqslant 270$), exclude the South Cap, and use the galaxy catalog "galaxy_DR12v5_CMASSLOWZTOT_North.fits." To minimize possible effects of redshift evolution in the clustering signal, we limit the sample in redshift range by using only spectroscopically identified CMASS galaxies with $0.44 < z < 0.64$. To minimize systematic uncertainties and facilitate interpretation, we require the galaxy tracer set (CMASS) to exhibit a constant clustering strength over the full redshift range of interest. Galaxy clustering studies (e.g., Meneux et al. 2009; Law-Smith & Eisenstein 2017) show that the clustering strength depends on

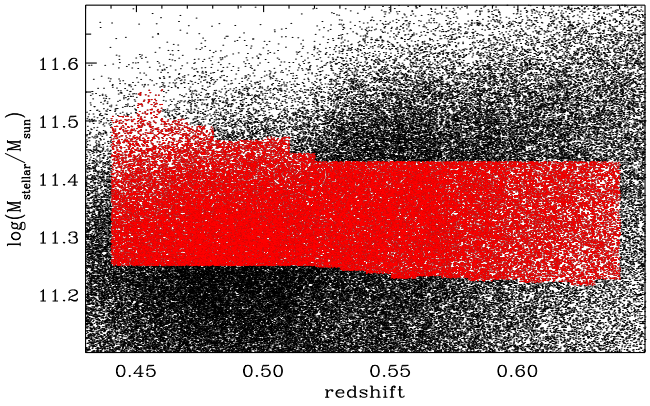

Figure 1. Stellar mass vs. redshift for the full spectroscopic CMASS sample (black data points) and the CMASS subsample (red) used for cross-correlation measurements with AGNs.

stellar mass in particular for red galaxies. Thus, restricting the stellar mass range will lead to a nearly constant clustering strength in a narrow redshift range.

Comparat et al. (2017) performed spectral fitting of stellar population models on all SDSS spectra classified as galaxies in DR14 (including CMASS and LRGs) and derived galaxy physical properties; stellar masses in particular are relevant here. Fits are performed with the full spectral fitting code Firefly[12] (Wilkinson et al. 2017) and the stellar population models of Maraston & Strömbäck (2011, hereafter M11), which are provided for several choices of stellar initial mass functions and input stellar library. We use their results for the M11-ELODIE population model, calculated assuming the ELODIE stellar library (Prugniel et al. 2007) for a Salpeter stellar initial mass function (Salpeter 1955). The CMASS stellar mass ($M_{\rm stellar}$) as a function of redshift is shown in Figure 1 (black and red data points). Initially, we limit the stellar mass to $11.25 < \log(M_{\rm stellar}/M_{\odot}) < 11.43$, which is a compromise between a narrow stellar mass range and maximizing the number of sources. The median stellar mass of this sample is $\langle \log(M_{\rm stellar}/M_{\odot})\rangle = 11.33$.

When we split the CMASS sample into low ($0.44 < z < 0.54$) and high ($0.54 \leqslant z < 0.64$) redshift subsamples, the high-z CMASS sample shows on average a slightly higher clustering strengths on scales $\gtrsim 1\ h^{-1}$ Mpc. This is because the median value of the stellar mass increases slightly from $z = 0.44$ to $z = 0.64$. This results from an incompleteness in the CMASS sample stellar mass as a function of redshift as reported in, e.g., Leauthaud et al. (2016) and Rodríguez-Torres et al. (2016; see their Figure 3). To remove this bias, we compute the median stellar mass in bins of $\Delta z = 0.01$ over the redshift range of $z = 0.44$–0.64 and add objects either below or above the primary chosen stellar mass range in each individual bin until each redshift bin has an identical median stellar mass of $\langle \log(M_{\rm stellar}/M_{\odot})\rangle = 11.33$. This results in the selection of 148,686 spectroscopic CMASS galaxies, as show in red in Figure 1.

As described in Appendix A we correct for fiber collisions in the spectroscopic sample when calculating the correlation function. This increases the number of objects in the final CMASS sample to 150,898 galaxies. We consider only the CMASS galaxy sample from the SDSS North Cap (~6940 deg^2). The median redshift is $\langle z\rangle = 0.53$ and the comoving number density is $(8.00 \pm 0.13) \times 10^{-5}\ h^3$ Mpc^{-3}. Uncertainties on the number densities are determined using jackknife resampling, the details of which are given in Section 4.2 below.

2.1.1. Random Catalogs

The computation of correlation functions requires a random catalog. We use the random catalogs provided by the SDSS consortium (e.g., Reid et al. 2016). The random catalogs for the CMASS sample in the North Cap can be found online.[13] As the data catalogs for the CMASS sample use weights to account for all observational biases (see Appendix A), the random catalogs can be used as provided.

For the random catalogs, we use 250 times as many objects as in the observed samples. This ensures that we minimize uncertainties due to statistical effects of the random catalog, in particular for pairs at the smallest scales measured. We verify that the randomly distributed objects fall within the same SDSS DR12 footprint as the observed CMASS galaxies.

As in Papers I–IV, the corresponding redshifts for the random objects are drawn from the smoothed redshift distribution of the observed CMASS sample by applying a least-squares (Savitzky & Golay 1964) low-pass filter. The same jackknife subarea definition is used as that for the observed sample (see Section 4.2).

2.2. Active Galactic Nuclei Samples

The goal of this paper is to compare the clustering properties of X-ray-selected and optically selected broad-line AGN (BLAGN) samples. SDSS is perfectly suited for this purpose, as it included follow-up spectroscopy of extragalactic X-ray sources and an optical AGN identification program based primarily on color selection. In addition, we aim to study AGN clustering properties as a function of various AGN parameters. The following subsections provide more details on the X-ray and optically selected AGN samples and how we create the different BLAGN subsamples.

2.2.1. X-Ray RASS/SDSS AGNs

The X-ray-selected AGN sample is based on SDSS-IV DR14 SPIDERS (SPectroscopic IDentification of eROSITA Sources; Blanton et al. 2017). The X-ray telescope eROSITA (Predehl et al. 2021) on board the SRG observatory (Sunyaev et al. 2021) was successfully launched in 2019 July. However, due to the delay of the launch, SDSS DR14 SPIDERS targets could not be selected using eROSITA. Instead the precursor ROSAT mission (Trümper 1982) was used as the main input for target selection. RASS (Voges et al. 1999) is an all-sky survey in the soft (0.1–2.4 keV) X-ray regime. Using this survey, Voges et al. (1999) and Voges et al. (2000) presented the RASS bright and faint source catalog, respectively. A goal of the ongoing SPIDERS project is to obtain highly complete and reliable optical identifications for these sources with the SDSS telescope.

We make use of SDSS DR14 and consider only X-ray sources that are listed in the revised version of the RASS catalog presented by Boller & Freyberg (2016; 2RXS). Several major improvements and bug fixes compared to the previous version of RASS resulted in the deepest and cleanest X-ray

[12] https://www.icg.port.ac.uk/firefly/

[13] https://data.sdss.org/sas/dr12/boss/lss/

all-sky survey collected by ROSAT. In particular, 2RXS aims for a significant reduction of the number of spurious sources.

We supplement the DR14 SPIDERS 2RXS sample (Coffey et al. 2019; Comparat et al. 2020) with RASS sources lying outside the eBOSS/DR14 footprint but within the footprint of earlier SDSS spectroscopic coverage. We cross-match the AllWISE counterparts to 2RXS sources (Salvato et al. 2018) to the SDSS Data Release 13 photometric catalog, choosing the brightest counterpart (in the r band) within a 3″radius of the AllWISE position. The optical counterparts are then matched to the SDSS DR14 optical spectroscopic catalog (Abolfathi et al. 2018) using a search radius of 1″.

The reported luminosities are 0.1–2.4 keV k-corrected rest-frame luminosities, assuming a photon index of $\Gamma = 2.4$. They are corrected for Galactic absorption. We restrict the X-ray-selected AGN sample to the same redshift range as our CMASS galaxy sample ($0.44 < z < 0.64$) and to the same SDSS footprint. This yields a total of ∼2130 in the North Cap ($100 \leqslant$ R.A. $\leqslant 270$). We apply an additional selection to this sample in Section 3.1 below and obtain a final sample of 1701 broad-line X-ray AGNs.

2.2.2. Optical SDSS AGNs

The optical AGN sample is drawn from the SDSS Quasar Catalog DR14 (Pâris et al. 2018), which contains all AGNs observed as part of SDSS I–IV. The newly discovered SDSS-IV/eBOSS AGNs arise from the target selection presented by Myers et al. (2015). Pâris et al. (2018) defined an AGN as an object with a luminosity of $M_i[z = 2] < -20.5$ mag that also has at least one emission line with FWHM > 500 km s^{-1} or has interesting or complex absorption features. Given the large number (526,356) of objects in the catalog, visual inspection of the optical spectra of these sources is not feasible. The automatic classification pipeline determines the redshift based on the maximum peak of the Mg II emission line, which is observable in eBOSS spectra from $z = 0.3$–2.5.

As with the X-ray-selected AGN sample, we limit the optical AGN sample to the same SDSS footprint and redshift range ($0.44 < z < 0.64$) as our CMASS galaxy sample. This results in a total of 11,298 optical AGNs in the North Cap. Note that we further down-select this sample in Section 3.1 and obtain 10,994 broad-line optical AGNs.

There is a significant overlap between the X-ray and optical AGN samples: 95.7% of the X-ray-selected AGNs are also selected by the optical AGN selection. However, the two samples do reflect different AGN selection criteria and AGN populations. The RASS sample is essentially flux-limited. The optical AGN sample is based on a heterogeneous AGN selection based on a combination of nonstellar optical color selection and radio point-source detection. As the host galaxy can contribute significantly to the total optical emission, there is a selection bias against detecting low-luminosity AGNs in galaxies where the optical host light is substantial.

Figure 2 shows the overlap between and differences in the two selection methods. The X-ray detected AGNs have on average higher $M_i(z = 2)$ values than the average of the optical BLAGN sample. However, there are also a substantial number of optical BLAGNs with very high $M_i(z = 2)$ values that are not detected in X-rays: 30% of optical BLAGNs brighter than $M_i(z = 2) = -24$ mag are not detected in X-rays. For BLAGNs brighter than $M_i(z = 2) = -25$ mag, this fraction increases to almost 50%. Given the substantial differences in these samples, we aim to test whether the different BLAGN selections lead to differences in the clustering properties of the samples.

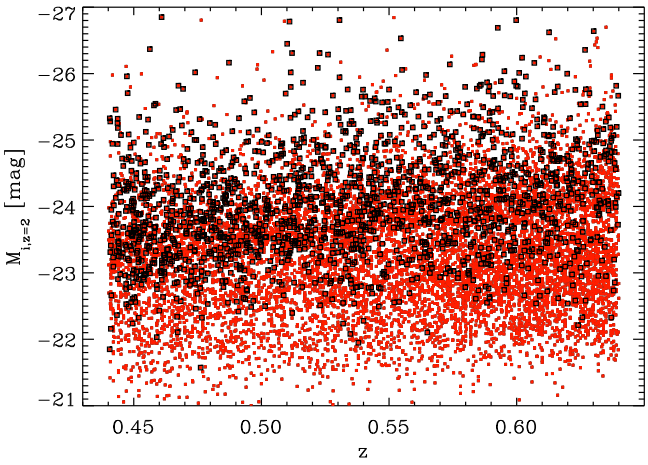

Figure 2. Comparison of the X-ray-selected (RASS/SDSS) BLAGN sample (black squares) and the optically selected (SDSS) BLAGN sample (red points), showing absolute i-band magnitude (k-corrected to $z = 2$) vs. redshift.

3. Creating Broad-line Active Galactic Nuclei Samples

For the X-ray-selected and optical AGN samples, we fit the individual SDSS optical spectra. In the redshift range of $0.44 < z < 0.64$, the Hβ line is always in the available SDSS spectral wavelength range, except for objects in which this wavelength range is masked out based as a result of quality checks. We use the Hβ line properties to include or exclude an object in our BLAGN samples. In Paper IV, we used the Hα line to make this distinction as the AGN sample originated from a lower redshift range ($0.16 < z < 0.36$). Using the Hβ line properties not only allows for the generation of a BLAGN sample but is also used to estimate the $M_{\rm BH}$ and $L/L_{\rm EDD}$. The details of the procedure are given in the following subsections.

3.1. Hβ Spectral Line Measurements

We model the spectral region around the Hβ line for all SDSS optical spectra. For the X-ray sample, we visually inspect each fit to verify its robustness and improve the fit if necessary. For the larger optical AGN sample, we visually inspect a subset, focusing on potential problematic cases.

In particular, the X-ray sample includes not only BLAGNs but narrow-line AGNs, inactive galaxies, and stars as well. We use the spectral class given by the SDSS pipeline (Bolton et al. 2012) as an initial estimate of the nature of the X-ray source. For objects classified as `QSO` or `BLAGN`, we fit a broad-line model to the SDSS spectrum. In other cases, we first test if a potential line with a peak S/N >3 per pixel is present at the location of Hβ. If so, we fit the spectrum with a narrow-line-only and a narrow+broad-line model. We use the latter model only if it leads to an improvement in the reduced χ^2 by at least 25%. This threshold is empirical and based on our visual quality checks of the fits. Otherwise we classify the object as a narrow-line object.

For the optical AGN sample, we initially fit every object with a broad-line model. For cases with a low amplitude of broad Hβ or cases identified during the visual inspection, we refit the spectrum with both a narrow-line and narrow+broad-line model and evaluate if the addition of a broad component is justified as described above. Based on this procedure, we

identify 1701 and 10,994 objects that require a broad-line component in the fit in the X-ray and the optical AGN DR14 sample, respectively.

Our procedure for continuum and emission line fitting uses code originally presented in Schulze et al. (2017, 2018). It builds on a Levenberg–Marquardt least-squares minimization as implemented in MPFIT (Markwardt 2009). We first correct the spectra for galactic extinction using the extinction map from Schlegel et al. (1998) and the reddening curve from Cardelli et al. (1989) and shift the spectra to their rest frame. We then fit and subtract a local pseudo-continuum over the wavelength windows 4435–4680 Å and 5100–5535 Å. The model consists of a power-law continuum and an optical iron template (Boroson & Green 1992), broadened by a Gaussian. The pseudo-continuum subtracted spectrum is then fit with an emission line model over the range 4700–5100 Å. For the narrow-line model, we fit the narrow Hβ and the narrow [O III] $\lambda\lambda$4959, 5007 lines, each fit by a single Gaussian. The [O III] $\lambda\lambda$4959, 5007 doublet is fit with two Gaussians for each line, one for the line core and one for the blue wing often present in this line (e.g., Mullaney et al. 2013). The two [O III] lines are coupled in shape and their line ratio is fixed to 3.0. The line width and velocity centroids of the core components are tied together for Hβ and the [O III] lines. In the broad-line model, we add a broad Hβ line, which we model with up to three Gaussians with FWHM $>$1000 km s^{-1} each. We stress that we do use these to capture the often non-Gaussian profile shape of the broad Hβ line and do not assign any physical nature to the individual components.

We measure the FWHM of the broad Hβ line (corrected for the instrumental resolution) and the continuum flux at 5100 Å from the best-fit model. In Figure 3 we show spectra and the best-fit models for six representative objects with typical S/Ns. For spectra with low S/Ns, the uncertainties and systematic errors on the line width measurements can become substantial, compared to the systematic uncertainty of $\sim$0.3 dex of the virial method to estimate black hole masses. Therefore, we use a lower S/N threshold for the sample, similar to Paper IV. We define the S/N over the Hβ range as the median S/N per pixel over the range 4750–4950 Å. In Appendix B we show that Hβ FWHM measurements with S/N $>$ 5 should be used to determine robust results and allow for a meaningful estimate of $M_{\rm BH}$. In Appendix C we compare our Hβ measurements with those from other studies and find good agreement. The broad-line X-ray and optically selected AGN samples used here (Hβ-S/N $>$ 5) have median S/N values of 14.1 and 10.8, respectively.

3.2. Estimating Black Hole Masses and Eddington Ratios

For BLAGNs, black hole masses can be estimated using the viral method (e.g., McLure & Jarvis 2002; Vestergaard & Peterson 2006). This technique builds on the assumption of virialized motions of the broad-line region (BLR) gas (Peterson & Wandel 2000), where the broad-line width serves as an estimate of the gas velocity, and uses an empirical scaling relation between BLR size and continuum luminosity (Kaspi et al. 2000; Bentz et al. 2009). The typical uncertainty on $M_{\rm BH}$ using the virial method for individual objects is $\sim$0.3–0.4 dex. The method is particularly powerful when studying the statistical properties of large samples of BLAGNs (e.g., McLure & Dunlop 2004; Kelly & Shen 2013; Schulze et al. 2015).

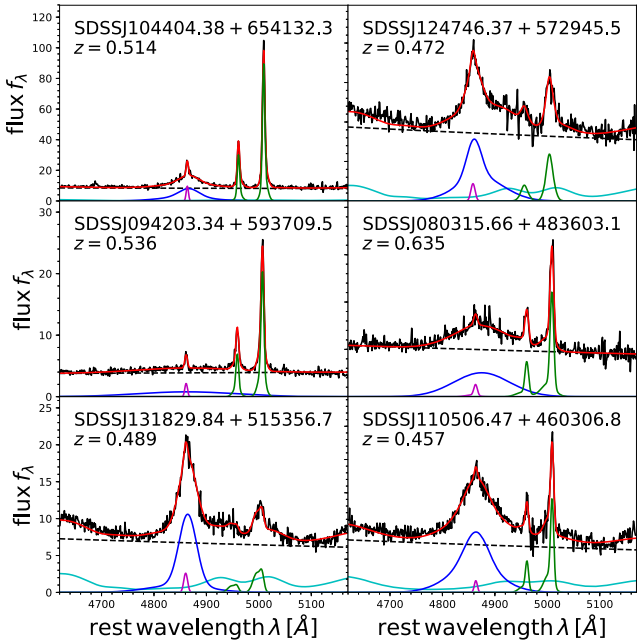

Figure 3. Example SDSS spectra (black solid line) of typical S/N sources and the best-fit models (red solid line) of the Hβ region. We show the individual model components, including a power law (black dashed line), the iron template (cyan line), the broad (blue) and narrow (magenta) Hβ lines, and the [O III] lines (green).

The virial method is most directly calibrated for the Hβ line; thus, this line typically provides the most reliable black hole mass estimate. The Mg II line, which is covered by the SDSS spectra in our sample, is also known to be a reliable black hole mass estimator (Trakhtenbrot & Netzer 2012; Mejía-Restrepo et al. 2016). However, the Mg II mass estimator is calibrated to Hβ, so when both lines are available (as in our sample), Hβ is the preferred choice. We therefore do not fit the Mg II line for this study. We estimate black hole masses from Hβ using the formula given by Vestergaard & Peterson (2006):

$$M_{\rm BH}\,({\rm H}\beta) = 10^{6.91}\left(\frac{L_{5100}}{10^{44}\ {\rm erg\ s^{-1}}}\right)^{0.5}\left(\frac{\rm FWHM}{1000\ {\rm km\ s^{-1}}}\right)^{2} M_{\odot}. \quad (1)$$

For the broad luminosity range of our AGN sample, the host galaxy contamination to the continuum luminosity L_{5100} is not negligible. Shen et al. (2011) showed that host galaxy contamination becomes significant at $L_{5100} < 10^{45}$ erg s^{-1}. We account for the host contribution in an average sense by applying the formula for the average host contamination given by Shen et al. (2011).

We estimate the bolometric luminosity for our sample from the (host-corrected) continuum luminosity L_{5100}. Specifically, we use a constant bolometric correction factor $\mathrm{BC}_{5100} = 7.0$ (Netzer & Trakhtenbrot 2007), which is consistent on average with the luminosity-dependent bolometric correction of Marconi et al. (2004) and excludes reprocessed emission from the mid-IR. Schulze et al. (2018) demonstrated the consistency of this bolometric correction factor with $L_{\rm bol}$ obtained by direct integration of the spectral energy distribution and other common bolometric luminosity indicators. Combining our estimates of $M_{\rm BH}$ and $L_{\rm bol}$ provides the Eddington ratio $L/L_{\rm EDD}$ for AGNs in our sample, where $L_{\rm EDD} \cong 1.3 \times 10^{38} (M_{\rm BH}/M_{\odot})$ erg s^{-1} is the Eddington luminosity.

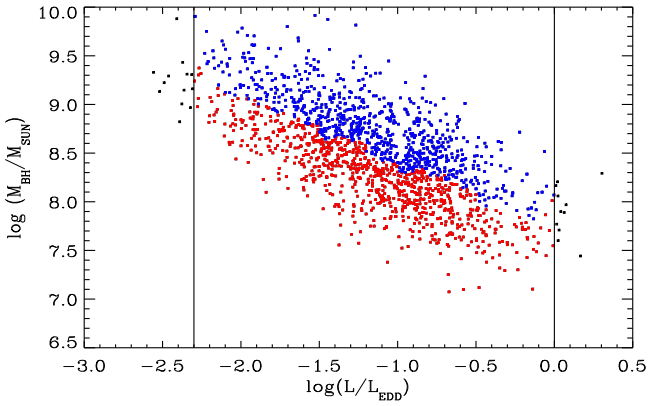

Figure 4. $M_{\rm BH}$ vs. $L/L_{\rm EDD}$ for broad-line X-ray RASS/SDSS AGNs with S/N at H$\beta \geqslant$5. Blue symbols show the high $M_{\rm BH}$ sample, while red symbols show the low $M_{\rm BH}$ sample (the two samples have identical distributions in $L/L_{\rm EDD}$). Vertical lines mark the restriction of the parameter space to remove extreme objects.

We also compute the absolute magnitude as the $z = 2$ k-corrected i-band magnitude for both the X-ray and the optical AGN samples following Richards et al. (2006) using the k-correction from their Table 4. This allows us to better compare the optical and X-ray AGN samples, as for the latter, no $M_i(z = 2)$ is provided. For the optical AGNs, we compare our $M_i(z = 2)$ values with those in Pâris et al. (2018) and find excellent agreement. In 68% of the sample, the magnitudes differ by less then 0.056 mag, and in 95% of the sample, they differ by less then 0.085 mag.

3.3. Defining Broad-line X-Ray AGN Subsamples

Due to the relatively low number of sources, we decide to split the X-ray-selected BLAGN sample into only two subsamples as a function of various AGN parameters. First we divide the sample into low and high X-ray luminosity subsamples at the median log $(L_{\rm X}/[{\rm erg\ s^{-1}}]) = 44.82$ of the full sample. The properties of all X-ray AGN samples as well as subsamples are given in Table 2.

The observed X-ray luminosity is a combination of the physical parameter $M_{\rm BH}$ and $L/L_{\rm EDD}$. However, as in other redshift ranges (see Paper IV), the RASS/SDSS AGNs do not uniformly populate the $L/L_{\rm EDD}$—$M_{\rm BH}$ plane (Figure 4). Higher $L/L_{\rm EDD}$ are usually found in AGNs with lower $M_{\rm BH}$. The absence of objects in the lower-left corner of the plane is an observational bias. To remove the correlation between $M_{\rm BH}$ and $L/L_{\rm EDD}$ and test the clustering properties of each AGN parameter independently, we create subsamples that depend on one parameter only, while the distribution of the second parameter in both subsamples is identical. This "matching" of the subsamples is a commonly used method in clustering measurements (e.g., Coil et al. 2009) and was used in Paper IV. Thus we split the AGN sample into low and high $M_{\rm BH}$ samples with identical distributions in $L/L_{\rm EDD}$ and vice versa. To do so, we first remove extreme objects by considering only objects with $-2.3 < \log(L/L_{\rm EDD}) < 0.0$ for the $M_{\rm BH}$ split and $7.4 < \log(M_{\rm BH}/M_{\odot}) < 9.6$ for the $L/L_{\rm EDD}$ split. We then determine the number of objects in each bin in the parameter we are matching on, using a bin width of 0.1 for both parameters. Then in each bin, we split the sample at the median value of this bin and allow multiple draws of objects, to result in an identical number of objects in the low and high subsamples in each bin. As an example, we show the matched

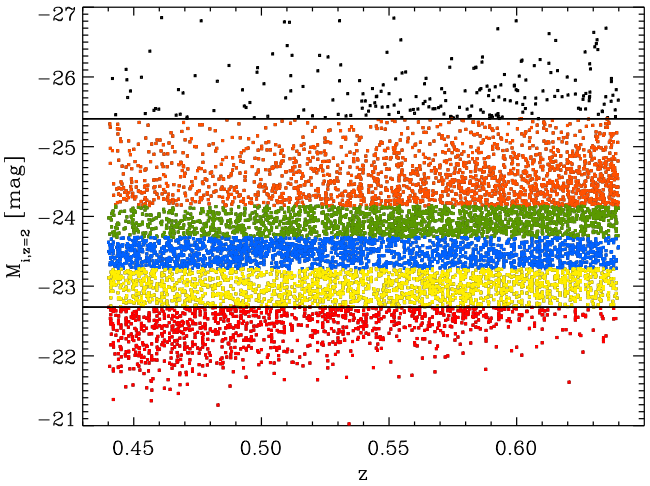

Figure 5. Absolute i-band magnitude (k-corrected to $z = 2$) vs. redshift for the broad-line optical AGNs with S/N at H$\beta \geqslant 5$. The different colors represent the different $M_i(z = 2)$ subsamples. The few brightest objects with $M_i(z = 2) < -25.4$ mag are not considered for the $M_i(z = 2)$ subsamples.

$M_{\rm BH}$ division in Figure 4. The $L/L_{\rm EDD}$ distribution of the low and high $M_{\rm BH}$ samples are identical.

We also split the sample at the median log $(L_{\rm Bol}/[{\rm erg\ s^{-1}}]) = 45.43$ and create low and high $L_{\rm Bol}$ subsamples. Finally, we split the X-ray BLAGN sample into faint and bright $M_i(z = 2)$ subsamples using the median $M_i(z = 2) = -24.07$ mag of the full AGN sample with reliable $M_{\rm BH}$ estimates.

3.4. Defining Broad-line Optical AGN Subsamples

For the optically selected SDSS AGNs, we follow a very similar approach as for the X-ray-selected AGNs. The major difference is that this sample has more than five times as many objects than the X-ray AGN sample. Thus we split the optical AGN sample in four, instead of two, subsamples in each parameter of interest.

We again create AGN subsamples with respect to $M_{\rm BH}$, $L/L_{\rm EDD}$ (with matched distributions in the other parameter of interest). We create these matched samples using objects with $-2.4 < \log(L/L_{\rm EDD}) < 0.0$ for the $M_{\rm BH}$ split and $7.0 < \log(M_{\rm BH}/M_{\odot}) < 9.6$ for the $L/L_{\rm EDD}$ split. We create four $L_{\rm Bol}$ subsamples by determining the values of $L_{\rm Bol}$ in the optical BLAGN sample (with reliable $M_{\rm BH}$ measurements) that correspond to 25%, 50%, and 75% objects of the full sample.

We also split the optical AGN sample in subsamples as a function of $M_i(z = 2)$. In order to have well-selected subsamples with similar redshift distributions, we limit the sample first at $M_i(z = 2) = -22.7$ mag and $M_i(z = 2) = -25.4$ mag. Figure 5 shows the four resulting subsamples, each of which have a similar number of objects. We keep the objects with $M_i(z = 2) > -22.7$ mag as an additional fifth M_i subsample. The properties of all optical AGN subsamples are listed in Table 2.

When comparing the X-ray and optical BLAGN samples (see Figure 6) in the space of the observed parameters $L_{\rm H\beta}$ versus FWHM (left panel) and the derived parameters $L/L_{\rm EDD}$ versus $M_{\rm BH}$ (right panel), the two samples cover a similar though not identical parameter space. Unlike our previous lower-redshift samples ($0.16 \leqslant z \leqslant 0.36$; Paper IV), here the X-ray-selected AGN sample does not extend to lower $L_{\rm H\beta}$. Instead the optical selection is able to detect more objects with lower Hβ luminosities. ROSAT's flux sensitivity is limited, and

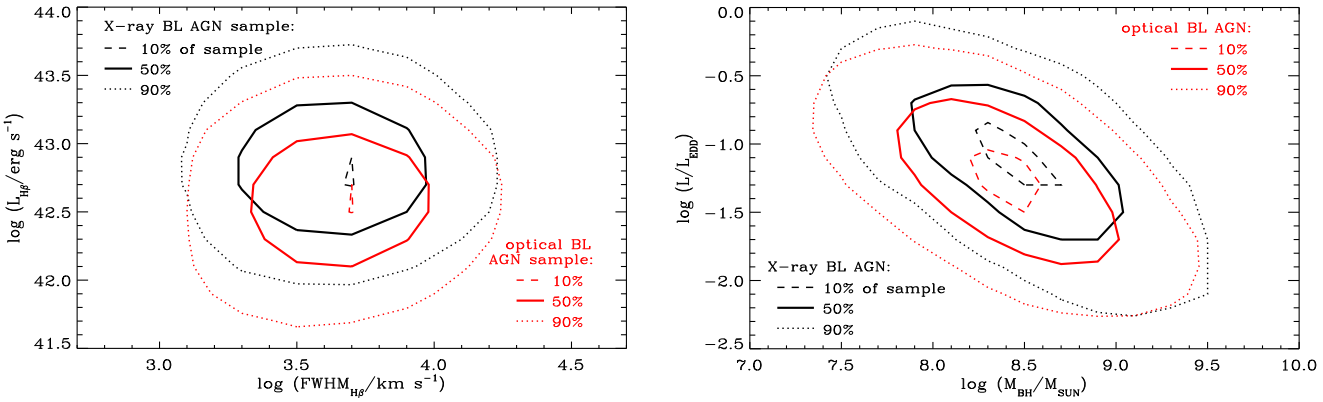

Figure 6. Comparison between broad-line X-ray-selected RASS/SDSS AGN (black lines) and broad-line optically selected SDSS AGNs (red lines) with S/N at Hβ >5. The contours show the location of 10% (dashed lines), 50% (solid lines), and 90% (dotted line) of the full sample, respectively. The left figure shows the observed parameters of the luminosity and FWHM of the Hβ line, while the right figure shows the derived parameters $L/L_{\rm EDD}$ and $M_{\rm BH}$. In both figures a boxcar smoothing with a width of two has been applied.

so with increasing redshift, even luminous AGNs will drop below the RASS flux limit. This is reflected in the total number of selected objects, as well as when directly comparing the number of objects with $\log\,(L_{\rm H\beta}/[{\rm erg}^{-1}]) \geqslant 43.5$, where we have 86 X-ray AGNs and 141 optical AGNs.

Differences in the observed parameter space naturally translate into differences in the derived $M_{\rm BH}$–$L/L_{\rm EDD}$ space (Figure 6, right panel). The X-ray AGN sample tends to select objects with somewhat higher $M_{\rm BH}$ and higher $L/L_{\rm EDD}$. This is not surprising as the X-ray luminosity is increasing from the lower-left to the upper-right corner in this parameter space. The optical sample extends to lower $M_{\rm BH}$ and lower $L/L_{\rm EDD}$.

4. Method

4.1. Clustering Measurements

We measure the two-point correlation function $\xi(r)$ (Peebles 1980), which measures the excess probability dP above a Poisson distribution. The ACF measures the spatial clustering of objects in the same sample, while the CCF measures the clustering of objects in two different samples. We use the same approach as described in detail in Papers I–IV. Here we only repeat the most essential elements of our method.

We use the correlation estimator of Davis & Peebles (1983) in the form

$$\xi(r) = \frac{\mathrm{DD}(r)}{\mathrm{DR}(r)} - 1, \tag{2}$$

where DD(r) is the number of data-data pairs with a separation r, and DR(r) is the number data-random pairs. Both pair counts have been normalized by the number density of data and random points. For our purposes, the use of this simple estimator has a number of major advantages and results in only a marginal loss in the S/N when compared to more advanced estimators (e.g., Landy & Szalay 1993). The estimator in Equation (2) requires the generation of a random catalog for the tracer set only.

To separate the effects of redshift distortions, the correlation function is measured as a function of two components of the separation vector between two objects, one perpendicular to (r_p) and the other along (π) the line of sight. $\xi(r_p, \pi)$ is thus extracted by counting pairs on a two-dimensional grid of separations r_p and π. We obtain the projected correlation function $w_p(r_p)$ by integrating $\xi(r_p, \pi)$ along the π-direction.

We measure r_p in the range of 0.05–40 h^{-1} Mpc in 15 logarithmic bins, identical to those used in Papers III and IV. We compute π in bins of 5 h^{-1} Mpc in the range $\pi =$ 0–200 h^{-1} Mpc. To derive $\pi_{\rm max}$, we compute $w_p(r_p)$ for a set of $\pi_{\rm max}$ ranging from 10–160 h^{-1} Mpc in steps of 10 h^{-1} Mpc. We then fit $w_p(r_p)$ over a r_p range of 0.35–30 h^{-1} Mpc with a fixed $\gamma = 1.9$ (based on Paper I) and determine the correlation length r_0 for the individual $\pi_{\rm max}$ measurements. With increasing $\pi_{\rm max}$, more clustering signal is included, though at some $\pi_{\rm max}$ value, the estimated $w_p(r_p)$ stops increasing and the uncertainty of $w_p(r_p)$ increases afterwards. For the CMASS galaxy ACF and all AGN–CMASS CCFs, the correlation signal saturates at $\pi_{\rm max,ACF} = 80$ h^{-1} Mpc and $\pi_{\rm max,CCF} = 40$ h^{-1} Mpc, respectively. Previous CMASS ACF studies also use $\pi_{\rm max,ACF} = 80$–100 h^{-1} Mpc (e.g., White et al. 2011; Guo et al. 2013; Nuza et al. 2013; Guo et al. 2015).

Spectroscopic BLAGN redshifts have on average larger uncertainties than spectroscopic redshifts of galaxies. Typically the redshift uncertainties are $\delta z \sim 0.01$. Since we are integrating over $\pi_{\rm max,CCF} = 40$ h^{-1} Mpc, these small redshift uncertainties have a negligible impact on the clustering signal.

4.2. Error Analysis

The error analysis is identical to that used in Papers I–IV. We use the jackknife resampling technique to estimate the measurement errors based on the covariance matrix M_{ij}, which reflects the degree to which bin i is correlated with bin j.

We divide the survey area into $N_{\rm T} = 100$ subsections, which have roughly an equal area of ~70 square degrees. At the median redshift of the CMASS sample ($\langle z \rangle = 0.55$), each subarea spans a physical scale at least four times larger than our largest scales studied in this paper.

The $N_{\rm T}$ jackknife-resampled correlation functions define the covariance matrix:

$$M_{ij} = \frac{N_{\rm T}-1}{N_{\rm T}} \left[\sum_{k=1}^{N_{\rm T}} (w_k(r_{p,i}) - \langle w(r_{p,i}) \rangle) \times (w_k(r_{p,j}) - \langle w(r_{p,j}) \rangle) \right]. \tag{3}$$

We calculate $w_p(r_p)$ $N_{\rm T}$ times, where each jackknife sample excludes one section; $w_k(r_{p,i})$ and $w_k(r_{p,j})$ are from the kth

jackknife samples of the CMASS ACF and AGN CCFs, respectively, and $\langle w(r_{p,i})\rangle$ and $\langle w(r_{p,j})\rangle$ are the averages over all of the jackknife samples. The uncertainties represent 1σ (68.3%) confidence intervals.

4.3. Halo Occupation Distribution Modeling

HOD modeling is a popular method for interpreting correlation function results. In this model the sample objects are assumed to be in DMHs where the average number of objects per halo follows a parameterized function of halo mass separately for the central halo and satellite halos. The correlation function can be modeled as a sum of the contribution of pairs from the same DMH (one-halo term) and different DMHs (two-halo term). We interpret our results using the HOD modeling following an approach similar to that presented in Papers II and IV as well as in Krumpe et al. (2018). We use the HOD approach to obtain linear bias parameters, as well as to investigate differences in the measured CCFs among various AGN subsamples with CMASS galaxies, probing differences beyond using the bias parameters alone.

As we do not intend to present full constraints of the AGN HODs in this paper, the HOD model of the AGN is deliberately designed to be simple. In order to enable historical comparisons with the results from our previous work, we use the same expressions for the b–$M_{\rm DMH}$ relation (Tinker et al. 2005) and the halo mass function (Sheth et al. 2001), as in our previous work. In Krumpe et al. (2018), we use an improved version of our code that takes into account the effects of halo-halo collisions and scale-dependent bias (Tinker et al. 2005). Practically, this removes the need for excluding the transition range between one-halo and two-term-dominated regimes in the HOD modelings (see Papers II–IV).

The outline of our approach is as follows:

1. We first apply the HOD modeling technique to the ACF of the CMASS galaxies and determine central and satellite HODs using a correlated χ^2-fit with a model with four free parameters. The number density constraint is also included. The best-fitting parameter search and the associated confidence regions are generated using a Markov Chain Monte Carlo (MCMC) method.
2. In order to model the CCF between the CMASS galaxies and AGN samples, two HODs are required: the HOD of the CMASS galaxies derived in the previous step and that of the AGN. As the CMASS galaxy sample is much larger than the AGN samples (and therefore the statistical significance of the CMASS galaxy ACF is much higher than that of the CMASS galaxy–AGN CCF), we use the best-fit CMASS galaxy HOD derived above for calculating the uncertainties of the AGN HOD. Due to the lower S/N of the CCF measurements between AGN and CMASS galaxies, some parameters remain unconstrained when applying our HOD approach. We therefore fix these parameters to reasonable values. We use an MCMC parameter search when there are three free parameters to fit. If we fit only two free parameters, we apply a simple grid search. Details are given below.

4.3.1. HOD of CMASS Galaxies

For the HOD modeling of the CMASS galaxy sample, we use the five-parameter model of Zheng et al. (2007):

$$\langle N_{\rm G,c}\rangle(M_{\rm DMH}) = \frac{1}{2}\left[1 + {\rm erf}\left(\frac{\log M_{\rm DMH} - \log M_{\rm min}}{\sigma_{\log M}}\right)\right]$$
$$\langle N_{\rm G,s}\rangle(M_{\rm DMH}) = \langle N_{\rm G,c}\rangle(M_{\rm DMH})\left(\frac{M_{\rm DMH} - M_0}{M_1'}\right)^{\alpha_s}, \quad (4)$$

where the model fit parameters are $\log M_{\rm min}$, $\sigma_{\log M}$, $\log(M_1'/M_{\rm min})$, and α_s (satellite slope). Since M_0 is poorly constrained for our sample, we fix this to $M_0 = 0$, reducing the number of free parameters to four. For $M_0 = 0$, the convention is to use the symbol M_1 (which is the halo mass at which $\langle N^s(M_{\rm DMH})\rangle = 1$) instead of M_1'. We therefore use the variable M_1 hereafter.

Best-fit parameters are searched in the range of $0.1 < r_{\rm p}[{\rm h}^{-1}{\rm Mpc}] < 40$ and by minimizing the correlated χ^2:

$$\chi^2 = \sum_{ij}\{[w_{\rm p}(r_{{\rm p},i}) - w_{\rm p}^{\rm mdl}(r_{{\rm p},i})]M_{ij}^{-1} \times [w_{\rm p}(r_{{\rm p},j}) - w_{\rm p}^{\rm mdl}(r_{{\rm p},j})]\} + (n_{\rm G} - n_{\rm G}^{\rm mdl})^2/\sigma_{n_{\rm G}}^2, \quad (5)$$

where the quantities from the model are indicated by a superscript "mdl," M_{ij} is the covariance matrix (Equation (3)), $n_{\rm G}$ is the number density of CMASS galaxies, and $\sigma_{n_{\rm G}}$ is the 1σ error. We find $n_{\rm G} = (8.00 \pm 0.18) \times 10^{-5}\ h^3\ {\rm Mpc}^{-3}$ over $0.44 < z < 0.64$, where the 1σ error is estimated using jackknife resampling.

The best-fit parameter search and determination of the confidence contours are made using an MCMC method with the MCMC-F90 library by Marko Laine[14], which we have modified and linked to our HOD model calculation software. Table 1 provides the best-fit parameters and their 90% confidence errors (or 95% upper limits).

4.3.2. HOD of AGN Samples

We fit HOD models to the CCFs between the CMASS galaxy and the AGN (sub)samples. To calculate the expected CCF $w_{\rm p}(r_{\rm p})$, we use the best-fit HOD of the CMASS galaxies derived above and a model of the AGN HOD. For the AGN samples, we use the same HOD form as for the galaxy HOD, with an additional global normalization factor:

$$\langle N_{\rm A,c}\rangle(M_{\rm DMH}) = f_{\rm A}\frac{1}{2}\left[1 + {\rm erf}\left(\frac{\log M_{\rm DMH} - \log M_{\rm min}}{\sigma_{\log M}}\right)\right]$$
$$\langle N_{\rm A,s}\rangle(M_{\rm DMH}) = \langle N_{\rm A,c}\rangle(M_{\rm DMH})\left(\frac{M_{\rm DMH}}{M_1}\right)^{\alpha_s}, \quad (6)$$

where $f_{\rm A}$ is the AGN fraction (duty cycle) among central galaxies at $M_{\rm DMH} \gg M_{\rm min}$; this global normalization factor scales both the central and satellite galaxies. For the AGN samples, $\sigma_{\log M}$ can be poorly constrained,[15] and therefore we

[14] http://helios.fmi.fi/lainema/mcmcf90/

[15] When we fit $\sigma_{\log M}$ as a free parameter, the constraints are poor, with the smallest χ^2-value at $\sigma_{\log M} \sim 0$.

Table 1
Best-fit HOD Parameters of the CMASS ACF

Fit Parameter	Best Fit	90% Confidence Range (5th–95th Percentiles)
$\log M_{\rm min}$	13.76	13.73–13.81
$\sigma_{\log M}$	0.63	0.59–0.68
$\log(M_1/M_{\rm min})$	0.91	0.85–0.98
$\alpha_{\rm s}$	1.46	1.29–1.58
b(linear)	2.24	2.21–2.28

fix this parameter to 0. In this case, the factor $\frac{1}{2}\left[1+\mathrm{erf}\left(\frac{\log M_{\rm DMH}-\log M_{\rm min}}{\sigma_{\log M}}\right)\right]$ becomes $\Theta(\log M_{\rm DMH}-\log M_{\rm min})$ where $\Theta(x)$ is a step function that has a value of 0 at $x<0$ and 1 at $x\geqslant 0$, respectively. Thus there are three free parameters for the AGN HODs: $\log M_{\rm min}$, $\log(M_1/M_{\rm min})$, and α. We note that the central HOD does not have to saturate at a constant value for AGN samples, unlike in the case of HODs for mass- or luminosity-thresholding galaxy samples, where it is usually assumed that the centers of the most-massive DMHs are occupied by a massive or luminous galaxy. Thus, in general, Equation (6) may be too restrictive for an AGN HOD, and it would be ideal to introduce separate high-mass slopes for central and satellite AGNs. A cosmological simulation-based forward model by Aird & Coil (2021) predicts that the central AGN HOD decreases at large halo masses in many AGN samples. Such cases cannot be fully represented by Equation (6). If the central HOD does decrease with increasing halo mass, forcing to fit using Equation (6) could cause a misestimation of $\alpha_{\rm s}$. However, using the simple form here provides a guide to the satellite HOD behavior and can highlight differences between different samples.

We do not use AGN density constraints for the χ^2-fits and parameter searches, as the various observational biases in the AGN selection make the number density estimation very uncertain. The value of $f_{\rm A}$, which sets the global normalization of the AGN HOD, does not affect the resulting CCF. $f_{\rm A}$ can be determined following the CCF fit using the AGN density constraint.

We apply the MCMC method for the AGN HOD parameter search to the CCFs between CMASS galaxies and the total broad-line X-ray and optical AGN samples. We repeat the analysis for objects with S/N at H$\beta\geqslant 5$. We fit the range of $0.2<r_{\rm p}[{\rm h}^{-1}\,{\rm Mpc}]<25$ and $0.1<r_{\rm p}[{\rm h}^{-1}\,{\rm Mpc}]<25$ for the X-ray and optical AGN samples, respectively. The lower bounds are determined by the requirement that both samples have 15 pairs or more in the smallest $r_{\rm p}$ bin. At $r_{\rm p}[{\rm h}^{-1}\,{\rm Mpc}]>25$, redshift space distortions (RSD) substantially affect the measured $w_{\rm p}(r_p)$ values. Measurements at $r_{\rm p}[{\rm h}^{-1}\,{\rm Mpc}]>25$ have minimal contribution to the power-law fits used to determine $\pi_{\rm max}$ as discussed above; therefore, we do not include them in the HOD model fits. The latest version of our HOD code accounts for RSD to the two-halo term based on the linear theory (Kaiser 1987) following the recipe by van den Bosch et al. (2013). Using it is computationally prohibitive for our MCMC chain searches. Instead we calculate the RSD corrected $w_{\rm p}(r_{\rm p})$ model for the best-fit parameters to determine the potential level of impact (Section 5).

4.3.3. Luminosity, M_{BH}, and L/L_{EDD} AGN Subsamples

One of the main goals of this work is to investigate the differences in AGN HOD properties as a function of AGN luminosity, $M_{\rm BH}$, $L/L_{\rm EDD}$, and M_i, for which we create AGN subsamples. The constraints on $M_1'/M_{\rm min}$ are poor when fitting the full X-ray-selected AGN sample. For the subsamples, we therefore fix $M_1'/M_{\rm min}$ to be equal to 5, and we check the sensitivity of the results to different values of this parameter. This reduces the number of fit parameters to the most fundamental ones of interest, namely $\log M_{\rm min}$ and α. Fixing $M_1'/M_{\rm min}$ to 10 or 30 only modifies the large-scale bias in most cases by less than ± 0.02. In the most extreme case, the change in bias is ± 0.05. Even in this extreme scenario, this systematic error is well within the 1σ uncertainty range of the bias.

The purpose of reducing the number of fit parameters is twofold. First, for these two parameters we do not need to use a computationally intensive MCMC for each subsample; we can use a two-dimensional grid of models in a tabular form to explore the confidence range. Second, with fewer free parameters we can highlight the differences in the HODs of the subsamples, as fixing the extra parameter may reduce the confidence regions in the two-parameter confidence contour plots by removing projection effects. As our purpose is to investigate the difference between samples, rather than obtaining full HOD constraints, comparing the confidence ranges in the plane of the two essential parameters, while holding other parameters fixed, is more demonstrative than comparing full confidence contour plot matrices in the full parameter space.

5. Results

We compute the CMASS galaxy ACF within $0.44\leqslant z<0.64$ and at a median stellar mass of $\langle\log(M_{\rm stellar}/M_\odot)\rangle=11.33$ (which is constant across the full redshift range). The best-fit HOD model parameters, including the large-scale bias, are given in Table 1. The measured ACF and the HOD results are shown in Figure 7.

We measure the CCFs between different X-ray and optical AGN samples and CMASS galaxies. As described above, we run the computationally intensive MCMC fitting for the full X-ray and optical AGN samples. For the AGN subsamples we determine the best fit based on a search in a two-dimensional grid. Figure 8 shows the resulting CCFs ($w_{\rm p}(r_p)$) and best-fit HOD models, as well as residuals from the fits, for the $\mathrm{SN}_{\mathrm{H}_\beta}>5$ samples. In each panel, the best-fit model corrected for the RSD effect is also shown, which demonstrates that the deviation of $w_{\rm p}(r_{\rm p})$ at the largest $r_{\rm p}$ can be accounted for by the RSD effect, though this effect is not included in the MCMC procedure due to the computational requirements. Confidence contour matrices for these results are shown in Figure 9, with dots representing the corresponding MCMC chain. We present the best-fit values in Table 3.

The confidence contours can differ from the concentration of the MCMC chain points, as the contours are determined from the minimum χ^2-values along the projections and not from the probabilities based on the marginal distributions of the MCMC points in the projected space. Results are also shown for the satellite fraction:

$$f_{\rm sat}=\frac{\int\langle N_{\rm A,s}\rangle(d\phi/d\log M_{\rm DMH})d\log M_{\rm DMH}}{\int(\langle N_{\rm A,c}\rangle+\langle N_{\rm A,s}\rangle)(d\phi/d\log M_{\rm DMH})d\log M_{\rm DMH}},\quad(7)$$

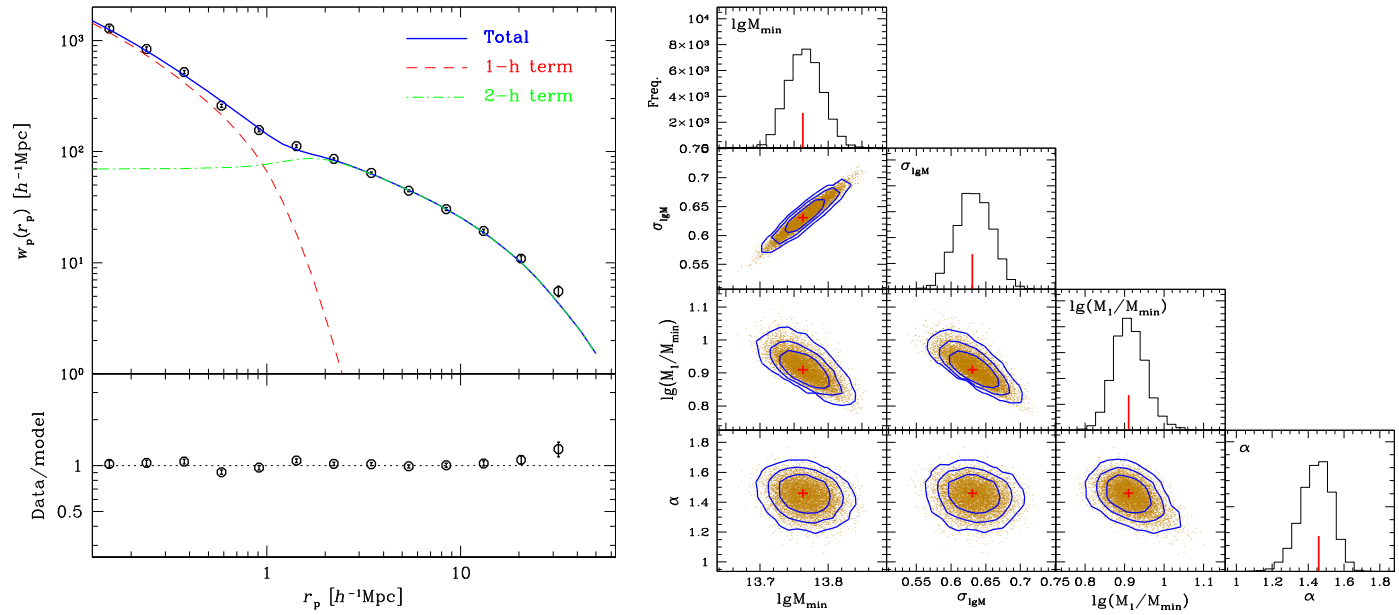

Figure 7. Left: the CMASS galaxy ACF (black circles) with 1σ error bars is shown, along with the best-fit HOD model (blue solid line). The one-halo and two-halo terms of the HOD model are shown with red short-dashed and green long-dashed lines, respectively. The lower panel shows the fit residuals in terms of the data/model ratio. Right: the MCMC points and confidence contour matrix of the CMASS HOD model parameters are shown, along with the marginal probability distribution of each parameter in the diagonal panels. The best-fit value in a two-parameter space is indicated with a red cross, while the best-fit value for one parameter is marked with a red vertical line. Individual dots indicate the MCMC chain points in the corresponding two-parameter space. The three contours in each panel correspond to $\Delta\chi^2 = \chi^2 - \chi^2_{\rm min}$ of 4.8, 7.9, and 12.1, below which 68%, 90%, and 98% of the chain points fall, respectively. In these figures, parameter names have been shortened for labeling purposes by omitting spaces and expressing log as lg.

where $d\phi/d\log M_{\rm DMH}$ is the halo mass function. The larger uncertainties derived for the X-ray-selected sample compared to the optical AGN sample are due to the smaller size of the X-ray sample.

Figure 10 (upper panel) shows the central and satellite HODs with 90% confidence ranges for the same samples as those in Figure 8. The sum of central and satellite AGN HODs is shown with their 90% confidence ranges in hatches. The lower panel shows the sum of the central and satellite HODs multiplied by the halo mass function, again with 90% confidence ranges shown in hatches.

5.1. Implications of the Halo Occupation Distribution Analysis

Before discussing our HOD analysis results in detail, we provide guidelines for interpreting the HOD parameterized model in Equation (6):

1. As the DMH mass distribution for AGN is very wide, the best-fit typical DMH should be interpreted carefully. It is useful to compare the typical DMH masses of different AGN samples to look for clustering trends; however, it should not be interpreted to imply that most AGNs reside in halos of this single mass.
2. A positive value of $\alpha_{\rm s} > 0$ implies that the number of AGNs in satellite galaxies increases with increasing $M_{\rm DMH}$, as might be expected, as this is the behavior of the galaxy HOD. On the other hand, $\alpha_{\rm s} < 0$ implies that AGNs in satellite galaxies are preferentially found in the lower-mass halos (i.e., modest richness groups) and are rare in high-mass halos (i.e., in rich groups and clusters).
3. By construction in the model, $\log M_1/M_{\rm min}$ becomes unconstrained for $\alpha_{\rm s} = 0$.
4. The two-halo term of the galaxy–AGN CCF is $\propto b_{\rm Gal} b_{\rm AGN}$, where the bias value is an indicator of some weighted mean host DMH mass.
5. There are two major constraints from the one-halo term: the amplitude of the clustering signal and the spatial extent of the one-halo-term-dominated region. The amplitude reflects the satellite-central and satellite-satellite pair counts within the same halos. The spatial extent reflects the maximum halo mass (i.e., the virial radius) that hosts a substantial satellite population.
6. The value of $f_{\rm sat}$ should not be over-interpreted, as it is highly model dependent, particularly the behavior of the model near $M_{\rm DMH} \sim M_{\rm min}$ where the halo mass function is large.

5.2. Findings from the Active Galactic Nuclei Grid Fitting Procedure

In addition to the MCMC method, we use the grid fitting procedure for all AGN (sub)samples.

The lower $r_{\rm p}$ value in each sample is determined such that there are at least 15 pairs in a bin. While for the full X-ray and optical AGN samples and most optical AGN subsamples, this is the case for $r_p \geqslant 0.1$–$0.3\ h^{-1}$ Mpc, for the X-ray AGN subsamples, this criterion is met for $r_p \geqslant 0.9\ h^{-1}$ Mpc. Thus we choose a conservative lower limit of $r_p = 0.9\ h^{-1}$ Mpc for all AGN samples where we use the grid fitting method and provide the results in Table 2. In this table we list the number of objects per AGN (sub)sample, the median redshift of the AGN sample, median absolute i-band magnitude (k-corrected for $z = 2$), median X-ray luminosity (rest-frame 0.1–2.4 keV, corrected for Galactic absorption), median black hole mass, median accretion ratio relative to Eddington, median bolometric luminosity, linear bias, typical DMH mass of the sample, and

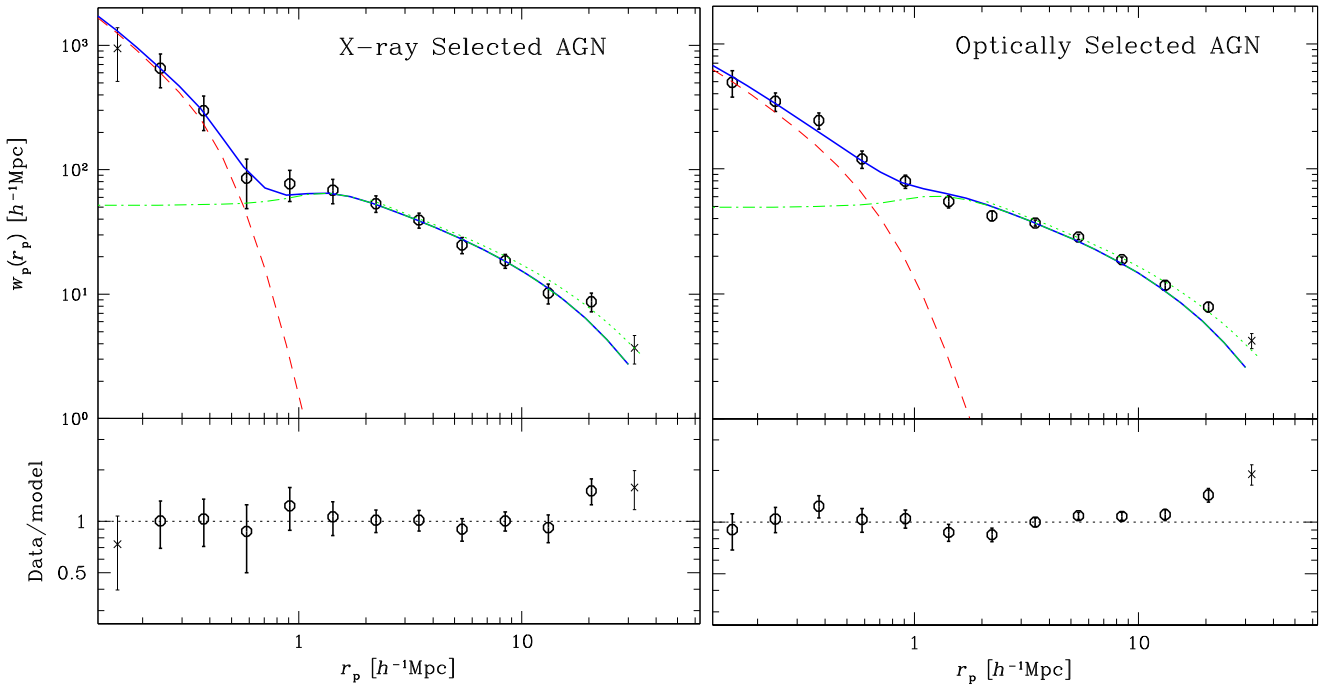

Figure 8. The measured CCF between the X-ray-selected (left) and the optically selected AGN sample (right) with the CMASS galaxy sample. In both cases, we show the AGN samples corresponding to "BL, Hβ-S/N > 5" in Table 2. The data points indicated by open circles and x-points represent the measurements included and excluded from the HOD model fitting process, respectively. The best-fit HOD model is shown with the one-halo (red dashed) term, two-halo (green dashed) term, and the sum of these terms (blue solid lines). The best-fit two-halo term model with the RSD correction is shown with a green short-dashed line.

mean DMH mass. The constraints on the last three quantities are derived from the HOD modeling approach and use the above mentioned fitting ranges. All typical DMH masses of the sample and mean DMH masses are computed for $z = 0.53$. The constraints on the bias, the typical DMH (derived from the bias), and mean DMH mass (which mainly depends on the bias) all effectively result from the two-halo term. Thus, we can obtain constraints without using data in the one-halo-dominated regime ($r_p < 0.9\,h^{-1}$ Mpc).

The results from the MCMC method show that the full broad-line X-ray and optical AGN samples have similar large-scale biases and HOD results. The largest difference is found for $\log(M_1/M_{\rm min})$, though it is only 1.1σ when considering the combined uncertainties. In particular the exclusion of the AGN for which the $M_{\rm BH}$ estimates are not as reliable does not significantly change the clustering results.

When comparing results from the MCMC and grid fitting approaches for the full X-ray and optical AGN samples, we obtain similar results (within the 1σ uncertainties). Differences arise due to having three free parameters in the MCMC method, while in the grid fitting method, two parameters are fit while the third is fixed at the same value for all samples. The grid fitting then results in tighter constraints on $\log M_{\rm min}$ and α_s than the MCMC approach.

Using the grid fitting procedure, we find differences in the large-scale clustering properties of some X-ray AGN subsamples in excess of the combined 2σ uncertainties. There is a weak L_X clustering dependence with the mean DMH masses, at a significance of 2.1σ, in that more X-ray luminous AGNs cluster more strongly than their lower-luminosity counterparts. We also find a 2.1σ positive $M_{\rm BH}$ clustering dependence in the X-ray AGN samples when considering the mean DMH masses. Among the optical AGN subsamples, we find a $>2\sigma$ difference in the clustering properties with respect to $L_{\rm Bol}$ (for details, see Section 6.7). For all other parameters (e.g., $L/L_{\rm EDD}$, M_i), the clustering properties in the optical and X-ray subsamples agree within $<2\sigma$. In general, the mean DMH mass is a similar quantity as the typical DMH, but the mean has contributions from the one- and two-halo terms while the typical DHM reflects the large-scale bias value, which has contributions from the two-halo term only.

6. Discussion

In discussing our findings we focus both on comparing our results with other studies as well as our previous work (in particular Papers III and IV) to draw conclusions on the evolution of BLAGN clustering properties across a redshift range of $z = 0.07$–0.64. The upper value of this redshift range corresponds to a lookback time of 6 Gyr, almost half of the lifetime of the universe. Our studies provide four independent measurements across this redshift range. Since the X-ray and optical AGN samples are generated by the same instruments (ROSAT and SDSS) and the methodology used (cross-correlation approach and HOD modeling) is identical, systematic effects are expected to be minimized compared to considering other studies that use different samples and methods. However, there are some differences across our studies, including (i) our HOD analysis improved over the years, (ii) different galaxy tracer sets are used, and (iii) the AGN samples from ROSAT/SDSS differ in some properties across this wide redshift range (e.g., lower luminosities at low redshift compared to high redshift).

6.1. X-Ray versus Optical Active Galactic Nuclei Clustering Properties

We first compare the clustering properties of the X-ray and optical AGN samples. Table 3 shows that the HOD parameters

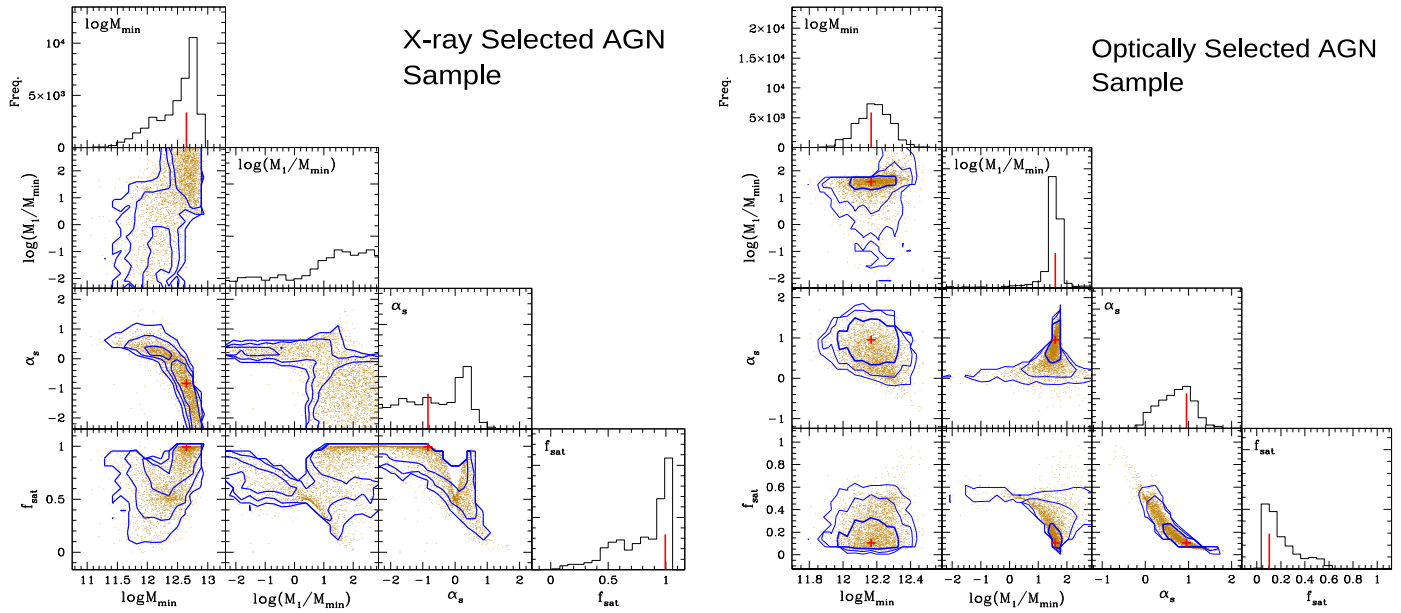

Figure 9. MCMC results with confidence contours for the parameters in Equation (6) from the CCF HOD analysis of the broad-line X-ray (left) and optically selected AGN (right) samples. Constraints on the satellite fraction $f_{\rm sat}$ are also derived from the model (see Equation (7)). In both cases, we use the sample with an S/N ratio at Hβ of >5. The nomenclatures are the same as those in Figure 7, except that $\Delta\chi^2$-levels are 3.6, 6.2, and 10.4 for the left panel and 4.5, 7.7, and 10.9 for the right panel, respectively. These correspond to 68%, 90%, and 98% of the chain points that fall because of the non-Gaussian probability distributions.

of the total X-ray and optical AGN samples agree well within the uncertainties, including for the samples with Hβ-S/N > 5. Figure 9 shows that due to differences in the sample sizes, the optical AGN sample has much tighter constraints than the X-ray AGN sample. The confidence ranges of these two samples have some overlap in the covered parameter spaces. An illustration of the overlap of the X-ray and optical AGN HODs is given in Figure 10.

Although the HOD results are not highly constraining due to the limited statistics (resulting from the relatively small AGN sample sizes), we are able to determine some salient characteristics. As shown in Figure 6, the X-ray AGN sample has on average higher-luminosity AGNs than the optical AGN sample, and the number density of the X-ray AGN sample is $\sim 1/5$ of that of the optical AGN sample. As the two-halo terms for the two samples are consistent with each other, the "typical" DMH masses are also consistent. However, there are differences in the one-halo term clustering properties, as seen in Figure 8. These differences are marginal, in that the 90% confidence ranges in the HOD parameter spaces as well as in HODs themselves overlap (Figures 9 and 10). However, for the X-ray sample, the preferred χ^2-values are in the $\alpha_{\rm s} < 0$ region, while $\alpha_{\rm s} < 0$ is almost excluded in the optical sample. As shown in Figure 8, the one-halo term of the X-ray-selected sample has a higher amplitude on small scales, and the scale at which the two-halo term dominates is lower. This points to higher $M_{\rm min}$ and lower $\alpha_{\rm s}$ for X-ray AGNs, where the AGNs in satellites are more common in halos near $M_{\rm min}$, and the occupation decreases for more-massive halos.

As discussed in Paper II, possible mechanisms for low $\alpha_{\rm s}$ include the decrease of the cross-section of satellite-satellite mergers triggering AGN activity (Makino & Hut 1997; Altamirano-Dévora et al. 2016) in high-velocity encounters in massive halos and ram pressure stripping of cold gas in the intracluster medium.

One caveat in interpreting $\alpha_{\rm s}$ is that an underlying assumption of our HOD model is that the radial distribution of satellite AGN follows the Navarro–Frenk–White halo mass density profile (Navarro et al. 1997) with the halo mass dependent concentration parameter of Zheng et al. (2007). It is possible that this assumption may not be valid for all AGN samples. An HOD model fit to the same data that assumes a different satellite radial profile would change the resulting $\alpha_{\rm s}$. However, such a model is beyond the scope of this paper and may be addressed when larger AGN samples such as those based on eROSITA become available in the future.

As mentioned above, our results indicate that X-ray-selected AGNs, in contrast to optically selected AGNs, contain a large population of satellites at $10^{13}\,h^{-1}M_{\odot}$. This is reflected in the $f_{\rm sat}$ distribution having higher values for the X-ray AGN sample. The marginal difference in the one-halo term behavior may be explained by X-ray selection identifying somewhat higher-luminosity AGNs than optical selection. However, the difference is statistically marginal and therefore we conclude that X-ray and optically selected BLAGN samples show very similar clustering properties in the redshift range $0.44 \leqslant z < 0.64$.

6.2. X-Ray versus Optical Active Galactic Nuclei Clustering as a Function of Redshift

In Paper III we found no statistically significant difference in the clustering properties of X-ray and optical AGNs at median redshifts of $z \sim 0.13$ (cross-correlation with SDSS main galaxies), $z \sim 0.27$ (cross-correlation with SDSS LRGs), and $z \sim 0.42$ (cross-correlation with the most-luminous SDSS LRGs). The amplitude and spatial extent of the one-halo term region are virtually identical in these lower-redshift ranges for X-ray and optically selected AGNs (see Figure 8 in Paper III). Taking the results of all independent redshift measurements into consideration, it appears that there are very similar bias values for X-ray and optical BLAGNs from very low redshift up to the redshift range studied of this work, with median $z \sim 0.53$.

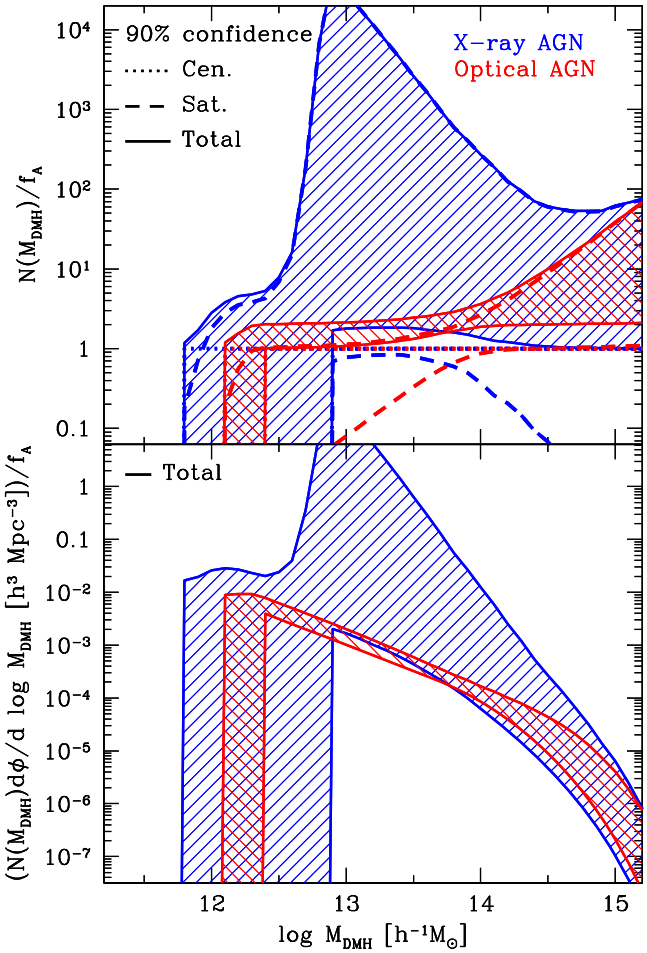

Figure 10. Comparison of the HODs determined for the X-ray (blue) and optical (red) AGN samples. Dotted, dashed, and solid lines show the 90% confidence ranges of the models in the MCMC chain evaluated at each $\log M_{\rm DMH}$ for $\langle N_{\rm A,c}\rangle(M_{\rm DMH})$, $\langle N_{\rm A,s}\rangle(M_{\rm DMH})$, and their sum, respectively. The total HOD constraint ranges are shown with hatches. Due to the functional form assumed for $\langle N_{\rm A,c}\rangle(M_{\rm DMH})$, the 5th and 95th percentile lines overlap with each other at high $M_{\rm DMH}$. Furthermore, the central, satellite, and total 90% limit lines also overlap at $M_{\rm DMH} = M_{\rm min}$ (vertical part). The y-axis in the upper panel shows $N(M_{\rm DMH})/f_{\rm A}$, such that large values may reflect a small $f_{\rm A}$. In the bottom panel, the product of the HOD and the DMH mass function $d\phi/d\,\log M_{\rm DMH}$ for the X-ray (blue) and optical (red) AGN samples (central+satellite) is shown. The large difference in the satellite term between these samples at $M_{\rm DMH} \sim 10^{13}\,h^{-1}\,M_{\odot}$ is due to very different $\alpha_{\rm s}$ constraints and is discussed in Section 5.1.

In each redshift range, the RASS X-ray selection and SDSS optical selection trace the full BLAGN population in different ways (see Figure 2). Figure 11 shows that the X-ray and optical luminosities of AGNs are correlated, though with substantial scatter. Thus, measuring clustering of optical AGNs alone does not necessarily allow one to make conclusions about the clustering of X-ray-selected AGNs, and vice versa.

In this work, we find statistically marginal differences in the HOD parameters between the X-ray and optical AGN samples due to differences in the one-halo term clustering properties. This is reminiscent of similar differences seen between low- and high-$L_{\rm X}$ AGNs as well as type I and type II AGNs in our previous work with the Swift/BAT+INTEGRAL/IBIS nearby AGN sample (Krumpe et al. 2018).

Despite possible differences in the one-halo term for X-ray and optical AGN samples at low redshift, their two-halo term clustering (and therefore large-scale bias) agrees very well. This is in contrast with previous X-ray and optical AGN clustering studies at higher redshifts ($z > 0.8$), which generally find that X-ray AGN samples are hosted by more-massive DMHs than optical AGN samples at the same redshift (see Porciani et al. 2004; Coil et al. 2007; Ross et al. 2009; Gilli et al. 2005, 2009; Coil et al. 2009; Allevato et al. 2011; Eftekharzadeh et al. 2015; Laurent et al. 2017). The differences in these results are likely due to a combination of different methodologies used in the conversion from $b_{\rm DMH}$ to $M_{\rm DMH}^{typ}$ in different studies, as well as differences in properties of the AGN samples (i.e., luminosity and BH mass) and in the properties of the galaxies hosting those AGNs.

Aird & Coil (2021) argued that AGN clustering results are most easily interpreted in terms of the relative bias of AGNs to well-characterized galaxy samples and are more challenging to interpret in terms of the absolute bias value alone. Comparing the clustering properties of (inactive) galaxy samples with matched properties as observed in the AGN samples (e.g., in stellar mass, redshift range, and star formation rate) reveals whether AGN clustering can be explained purely by the known galaxy-halo connection or whether the presence of AGNs in the center of a galaxy alters the clustering signal. Current measurements using this relative bias approach do find that the AGN clustering signal can be produced by inactive galaxies closely matched to the AGN in spectral class, stellar mass, and redshift (e.g., Mendez & Coil 2016; Mountrichas et al. 2019; Krishnan et al. 2020). Measuring host galaxies properties such as stellar mass in the most-luminous BLAGNs can be very challenging, making a relative bias measurement difficult. Alternatively, galaxy-galaxy lensing measurements can provide constraints on the $M_{\rm DMH}$ of the individual AGN host galaxies. Semiempirical modeling suggests a halo mass distribution for X-ray-selected AGNs that peaks at $M_{\rm DMH} \sim 10^{12}\,h^{-1}\,M_{\odot}$ with a tail extending to higher halo masses (Leauthaud et al. 2015; Georgakakis et al. 2019). This tail shifts the average halo mass to higher values than $M_{\rm DMH} \sim 10^{12}\,h^{-1}\,M_{\odot}$. In addition, the HOD modeling of the one-halo term should be improved to allow for distributions beyond a single power law. Equation (6) could be adjusted to allow for a more complex halo mass distribution of AGNs. Ideally the model would allow for different slopes at different halo masses. However, the challenge for such models would be the limited S/N of current AGN clustering measurements, such that a more flexible model would result in poor constraints on additional HOD parameters.

6.3. L_X Clustering Dependence of X-Ray-selected Active Galactic Nuclei

We find a weak and marginal clustering dependence on luminosity for X-ray-selected BLAGNs at a 2.1σ confidence level ($0.44 < z < 0.64$), in that higher-luminosity X-ray AGNs have a higher mean DMH mass than lower-luminosity AGNs. Interestingly, we previously discovered weak, positive, and marginally significant clustering dependences with $L_{\rm X}$ in two lower-redshift ranges ($0.07 < z < 0.16$, $0.16 < z < 0.36$). Considering the detection of a weak and tentative $L_{\rm X}$ clustering dependence in three independent redshift ranges provides stronger evidence for the existence of this positive but weak correlation. We note that our X-ray-selected AGN sample is drawn from a soft (0.1–2.4 keV) X-ray band, such that moderately X-ray absorbed AGNs will be missed by our selection. In Paper IV, we show with cosmological simulations that a weak $L_{\rm X}$ dependence of the clustering is only expected

Table 2
Properties of the AGN Samples and Derived HOD Model Quantities Using Grid Fitting

Sample Name	Number of Objects	Median z	Median $M_i(z=2)$	Median $\log L_X$	Median $\log M_{BH}$	Median $\log L/L_{EDD}$	Median $\log L_{Bol}$	$b(z)$ (HOD)	$\log M_{DMH}^{typ}$ ($h^{-1}\,M_\odot$)	$\log\langle M_{DMH}\rangle$ ($h^{-1}\,M_\odot$)
X-ray Broad-line AGN—RASS/SDSS, North Cap only										
Total BL sample	1701	0.53	−24.03	44.82	8.48	−1.14	45.43	$1.37^{+0.12}_{-0.13}$	$12.80^{+0.16}_{-0.20}$	$12.96^{+0.12}_{-0.19}$
BL, Hβ-S/N>5	1632	0.53	−24.07	44.82	8.49	−1.14	45.45	$1.35^{+0.14}_{-0.11}$	$12.77^{+0.19}_{-0.17}$	$12.92^{+0.15}_{-0.19}$
Low L_X	816	0.50	−23.76	44.66	8.39	−1.19	45.28	$1.20^{+0.16}_{-0.14}$	$12.52^{+0.26}_{-0.30}$	$12.65^{+0.25}_{-0.29}$
High L_X	816	0.55	−24.43	45.00	8.60	−1.06	45.62	$1.55^{+0.14}_{-0.21}$	$13.03^{+0.15}_{-0.27}$	$13.27^{+0.09}_{-0.14}$
Low M_{BM}	833	0.51	−23.64	44.72	8.23	−1.14	45.21	$1.24^{+0.16}_{-0.15}$	$12.60^{+0.24}_{-0.32}$	$12.71^{+0.23}_{-0.28}$
High M_{BM}	833	0.55	−24.63	44.93	8.75	−1.14	45.71	$1.57^{+0.18}_{-0.16}$	$13.05^{+0.19}_{-0.19}$	$13.27^{+0.12}_{-0.13}$
Low L/L_{EDD}	829	0.51	−23.62	44.73	8.49	−1.42	45.21	$1.42^{+0.18}_{-0.13}$	$12.87^{+0.22}_{-0.19}$	$12.97^{+0.20}_{-0.17}$
High L/L_{EDD}	827	0.54	−24.63	44.92	8.49	−0.83	45.71	$1.28^{+0.15}_{-0.18}$	$12.66^{+0.22}_{-0.34}$	$12.93^{+0.19}_{-0.31}$
Low L_{Bol}	817	0.51	−23.60	44.71	8.35	−1.31	45.19	$1.42^{+0.16}_{-0.18}$	$12.87^{+0.19}_{-0.27}$	$12.97^{+0.17}_{-0.24}$
High L_{Bol}	815	0.55	−24.64	44.94	8.62	−0.93	45.71	$1.35^{+0.16}_{-0.17}$	$12.77^{+0.21}_{-0.29}$	$13.10^{+0.13}_{-0.21}$
Faint M_i	815	0.51	−23.58	44.71	8.36	−1.30	45.19	$1.33^{+0.16}_{-0.17}$	$12.74^{+0.22}_{-0.30}$	$12.84^{+0.22}_{-0.25}$
Luminous M_i	817	0.55	−24.64	44.94	8.62	−0.94	45.71	$1.44^{+0.14}_{-0.17}$	$12.90^{+0.16}_{-0.26}$	$13.08^{+0.13}_{-0.25}$
Optical Broad-line AGN (Paris et al. sample)—SDSS, North Cap only										
Total BL sample	10,994	0.56	−23.37	⋯	8.35	−1.31	45.14	$1.28^{+0.04}_{-0.04}$	$12.66^{+0.06}_{-0.06}$	$12.89^{+0.08}_{-0.05}$
BL, Hβ-S/N>5	8889	0.55	−23.58	⋯	8.40	−1.26	45.24	$1.37^{+0.07}_{-0.06}$	$12.80^{+0.10}_{-0.09}$	$12.99^{+0.04}_{-0.08}$
0%–25% M_{BH}	2243	0.52	−22.78	⋯	7.93	−1.26	44.81	$1.29^{+0.08}_{-0.09}$	$12.68^{+0.12}_{-0.16}$	$12.92^{+0.11}_{-0.20}$
25%–50% M_{BH}	2243	0.54	−23.40	⋯	8.29	−1.26	45.13	$1.39^{+0.10}_{-0.10}$	$12.83^{+0.13}_{-0.15}$	$13.08^{+0.09}_{-0.13}$
50%–75% M_{BH}	2243	0.55	−23.82	⋯	8.51	−1.26	45.36	$1.42^{+0.09}_{-0.11}$	$12.87^{+0.11}_{-0.16}$	$12.96^{+0.13}_{-0.13}$
75%–100% M_{BH}	2243	0.57	−24.43	⋯	8.82	−1.26	45.64	$1.39^{+0.13}_{-0.12}$	$12.83^{+0.17}_{-0.19}$	$13.15^{+0.09}_{-0.12}$
0%–25% L/L_{EDD}	2242	0.53	−22.82	⋯	8.40	−1.68	44.84	$1.29^{+0.11}_{-0.11}$	$12.68^{+0.16}_{-0.20}$	$13.05^{+0.11}_{-0.10}$
25%–50% L/L_{EDD}	2242	0.54	−23.37	⋯	8.40	−1.37	45.15	$1.50^{+0.10}_{-0.12}$	$12.97^{+0.12}_{-0.15}$	$13.05^{+0.12}_{-0.12}$
50%–75% L/L_{EDD}	2242	0.55	−23.82	⋯	8.40	−1.14	45.37	$1.50^{+0.09}_{-0.12}$	$12.97^{+0.11}_{-0.15}$	$13.06^{+0.11}_{-0.14}$
75%–100% L/L_{EDD}	2242	0.56	−24.47	⋯	8.40	−0.82	45.66	$1.33^{+0.11}_{-0.10}$	$12.74^{+0.16}_{-0.16}$	$12.93^{+0.14}_{-0.17}$
0%–25% L_{Bol}	2223	0.52	−22.73	⋯	8.11	−1.47	44.80	$1.30^{+0.09}_{-0.12}$	$12.70^{+0.13}_{-0.22}$	$12.98^{+0.12}_{-0.14}$
25%–50% L_{Bol}	2223	0.55	−23.35	⋯	8.35	−1.35	45.12	$1.36^{+0.13}_{-0.08}$	$12.78^{+0.18}_{-0.12}$	$13.03^{+0.10}_{-0.11}$
50%–75% L_{Bol}	2222	0.55	−23.83	⋯	8.47	−1.22	45.37	$1.53^{+0.13}_{-0.04}$	$13.01^{+0.14}_{-0.05}$	$13.08^{+0.14}_{-0.04}$
75%–100% L_{Bol}	2221	0.57	−24.52	⋯	8.64	−1.01	45.67	$1.31^{+0.09}_{-0.13}$	$12.71^{+0.13}_{-0.23}$	$13.09^{+0.09}_{-0.15}$
$M_i > -22.7$	1097	0.50	−22.44	⋯	8.05	−1.48	44.69	$1.33^{+0.10}_{-0.12}$	$12.74^{+0.14}_{-0.20}$	$13.10^{+0.11}_{-0.14}$
$-22.7 < M_i < -23.25$	1853	0.55	−23.01	⋯	8.27	−1.41	44.96	$1.30^{+0.13}_{-0.12}$	$12.7^{+0.18}_{-0.22}$	$12.85^{+0.16}_{-0.13}$
$-23.25 < M_i < -23.70$	1997	0.53	−23.48	⋯	8.40	−1.32	45.20	$1.55^{+0.08}_{-0.13}$	$13.03^{+0.09}_{-0.16}$	$13.15^{+0.07}_{-0.14}$
$-23.70 < M_i < -24.15$	1871	0.56	−23.91	⋯	8.47	−1.21	45.40	$1.39^{+0.10}_{-0.13}$	$12.83^{+0.13}_{-0.20}$	$13.03^{+0.11}_{-0.17}$
$-24.15 < M_i < -25.4$	1853	0.55	−24.51	⋯	8.58	−1.03	45.66	$1.33^{+0.15}_{-0.08}$	$12.74^{+0.21}_{-0.12}$	$12.94^{+0.14}_{-0.18}$

Notes. All samples span a redshift range of $0.44 < z < 0.64$. For the HOD analysis of all (sub)samples presented in this table, we use a common, conservative fitting range of $r_p \geqslant 0.9\ h^{-1}$ Mpc. All bias values are computed at $z = 0.53$.

for the most-luminous AGN while the more moderate or weak L_X AGNs are not expected to exhibit an L_X dependence of the clustering properties. Aird & Coil (2021) also presented constraints on DMH mass distribution as a function of L_X and have results for very luminous AGNs that are consistent with our findings.

Figure 12 shows that there is not a simple continuous function of bias with L_X that is independent of redshift; what is observed is that AGNs with the same L_X show different clustering strengths at different redshifts. Within any redshift range, the most X-ray luminous AGNs have a similar high typical DMH mass of $M_{DMH} \sim 10^{13}\,h^{-1}\,M_\odot$. Within each individual redshift range, the lower L_X AGNs, being ∼5 times less luminous, have a typical $M_{DMH} \sim 10^{12.7}\,h^{-1}\,M_\odot$. There may be a tentative trend of lower DMH mass with increasing redshift for AGNs at a given X-ray luminosity.

To further investigate this observation, we compare the number density of AGNs at a given luminosity with that of DMHs at the corresponding typical halo mass. The ratio of these densities represents a "duty cycle," or the fraction of halos that contain an AGN. In principal, if a halo contains more than, for example, two AGNs at the same time, these count as two. However, as seen below, the duty cycle is much less than one, and such cases are rare. Here we compare the AGN duty

Table 3
Best-fit HOD Parameters of the Full AGN Samples Using MCMC

Sample Name	$b(z)$ (HOD, MCMC)	$\log M_{\rm DMH}^{\rm typ}$ ($h^{-1}\,M_\odot$)	$\log\langle M_{\rm DMH}\rangle$ ($h^{-1}\,M_\odot$)	$\log M_{\rm min}$ ($h^{-1}\,M_\odot$)	$\alpha_{\rm s}$	$\log(M_1/M_{\rm min})$
X-Ray Broad-line AGN—RASS/SDSS, North Cap only						
Full BL sample	$1.43^{+0.08}_{-0.16}$	$12.88^{+0.10}_{-0.20}$	$12.53^{+0.20}_{-0.33}$	$12.98^{+0.09}_{-0.10}$	$-0.21^{+0.50}_{-1.15}$	$1.07^{+1.19*}_{-1.05}$
Hβ-S/N>5	$1.42^{+0.09}_{-0.13}$	$12.89^{+0.11}_{-0.30}$	$12.97^{+0.10}_{-0.11}$	$12.54^{+0.19}_{-0.42}$	$-0.35^{+0.52}_{-1.1}$	$0.97^{+1.26*}_{-1.06}$
Optical Broad-line AGN (Paris et al. sample)—SDSS, North Cap only						
Full BL sample	$1.24^{+0.04}_{-0.04}$	$12.72^{+0.07}_{-0.08}$	$12.90^{+0.06}_{-0.06}$	$11.99^{+0.10}_{-0.11}$	$0.99^{+0.28}_{-0.31}$	$1.60^{+0.12}_{-0.18}$
Hβ-S/N>5	$1.32^{+0.05}_{-0.05}$	$12.72^{+0.06}_{-0.06}$	$12.93^{+0.06}_{-0.06}$	$12.20^{+0.09}_{-0.11}$	$0.54^{+0.43}_{-0.38}$	$1.55^{+0.18}_{-0.38}$

Note. The quoted best-fit value is the 50th percentile (median) of the MCMC parameter distribution, and the uncertainties are 68% confidence values for one parameter, derived from the distribution of the MCMC chain. The fitting ranges for the full samples are $0.2 < r_p < 25$ and $0.1 < r_p < 25$ [h^{-1} Mpc] for the X-ray and optical AGN samples, respectively. An asterisk (*) for the error value indicates that it is pegged at a parameter search limit.

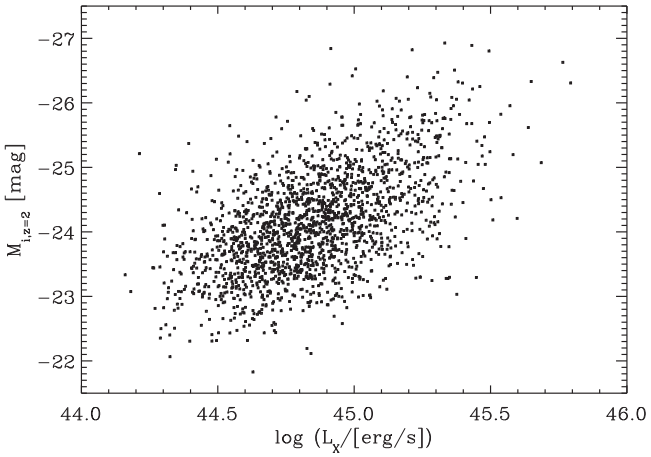

Figure 11. Comparison between the X-ray-selected (RASS/SDSS) BLAGN sample and the optically selected (SDSS) BLAGN sample. Absolute i-band magnitude (k-corrected to $z = 2$) is shown vs. rest-frame X-ray luminosity (0.1–2.4 keV) for X-ray-selected BLAGNs with S/N at H$\beta > 5$.

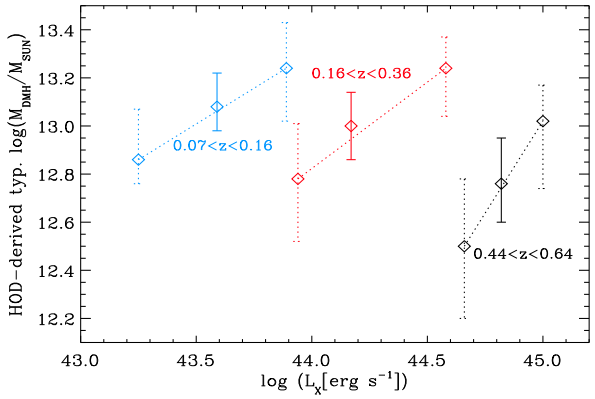

Figure 12. Typical DMH mass (derived from HOD modeling and grid fitting approach) as a function of 0.1–2.4 keV luminosity in independent redshift ranges (shown with different colors). Data points with the solid error bars show the full samples, while the data points with dashed error bars display the respective subsamples split by X-ray luminosity.

cycles between the highest- and lowest-redshift bins shown in Figure 12. We estimate the duty cycle by

$$\text{duty cycle} \sim \frac{d\,\phi_{\rm X}/d\,\log L_{\rm X}}{d\,\phi_{\rm DMH}/d\,\log M_{\rm DMH}} \cdot \left| \frac{d\,\log L_{\rm X}}{d\,\log M_{\rm DMH}} \right|, \quad (8)$$

i.e., the ratio between the X-ray luminosity function (XLF) and the corresponding DMH mass function. The XLF ($d\,\phi_{\rm X}/d\,\log L_{\rm X}$) is obtained from the 0.5–2 keV XLF (Hasinger et al. 2005; Miyaji et al. 2001) converted to our 0.1–2.4 keV band assuming a photon index of $\Gamma = 2.4$. The DMH mass function ($d\,\phi_{\rm DMH}/d\,\log M_{\rm DMH}$) is from Sheth et al. (2001) and is implemented in our HOD code. The factor $|d\,\log L_{\rm X}/d\,\log M_{\rm DMH}|$ is estimated from the slope for the given redshift bin in Figure 12.

For our $z \sim 0.53$ sample with $M_{\rm DMH} \sim 10^{12.8}\,h^{-1}\,M_\odot$, the estimated duty cycle is $\sim 1 \times 10^{-3}$, i.e., 0.1% of the DMHs at this halo mass could contain a BLAGN. Using the DMH mass growth rate of Fakhouri et al. (2010), the descendants of halos of mass $M_{\rm DMH} \sim 10^{12.8}\,h^{-1}\,M_\odot$ at $z \sim 0.53$ have $M_{\rm DMH} \sim 10^{13.0}\,h^{-1}\,M_\odot$ at $z \sim 0.13$. The duty cycle for these descendants (at $z \sim 0.13$) is estimated to be $\sim$2%. Thus, roughly speaking, the duty cycle represented by our high-$L_{\rm X}$ $z \sim 0.13$ sample at $M_{\rm DMH} \sim 10^{13.2}\,h^{-1}M_\odot$ DMHs has increased by an order of magnitude compared to their progenitor DMHs at $z \sim 0.53$.

There are caveats in interpreting our results in this manner. We assume that the observed slope of the $\log M_{\rm DMH}$–$\log L_{\rm X}$ relation at each redshift range can be extended to unprobed luminosities. The error on the slope is large, and it is not guaranteed that the observed relation applies beyond the observed luminosity range. In particular, at $z \sim 0.53$, AGNs with a luminosity of $L_{0.1-2\,\rm keV} \lesssim 10^{44} h_{70}^{-2}$ erg s^{-1} are below the RASS flux limit and thus not included in our sample. Those AGNs may well reside in $10^{12.5}\,h^{-1}\,M_\odot$ DMHs. This would result in a smaller $|d\,\phi_{\rm DMH}/d\,\log M_{\rm DMH}|$ and thus a larger duty cycle. Future analysis of AGN samples collected with *eROSITA* will allow us to explore the typical DMH masses of luminosity- and redshift-defined AGN samples to compare the differences in duty cycles in this space with unprecedented precision.

6.4. M_i Clustering Dependence of Optically Selected Active Galactic Nuclei

We do not find a clear clustering dependence of the optically selected AGNs with $M_{\rm i}$ (see Table 2). The subsample with $-23.25 < M_{\rm i} < -23.70$ deviates the most from other subsamples but at a difference of only $\sim 1.4\sigma$. Other than the $M_{\rm i} > -22.7$ mag subsample, all samples have similar redshift distributions. To remove differences in the redshift distributions completely, we create redshift-matched subsamples (except for the subsample $M_{\rm i} > -22.7$ mag) and analyze their clustering properties. The bias values for these samples vary within their 1σ uncertainties, such that no significant

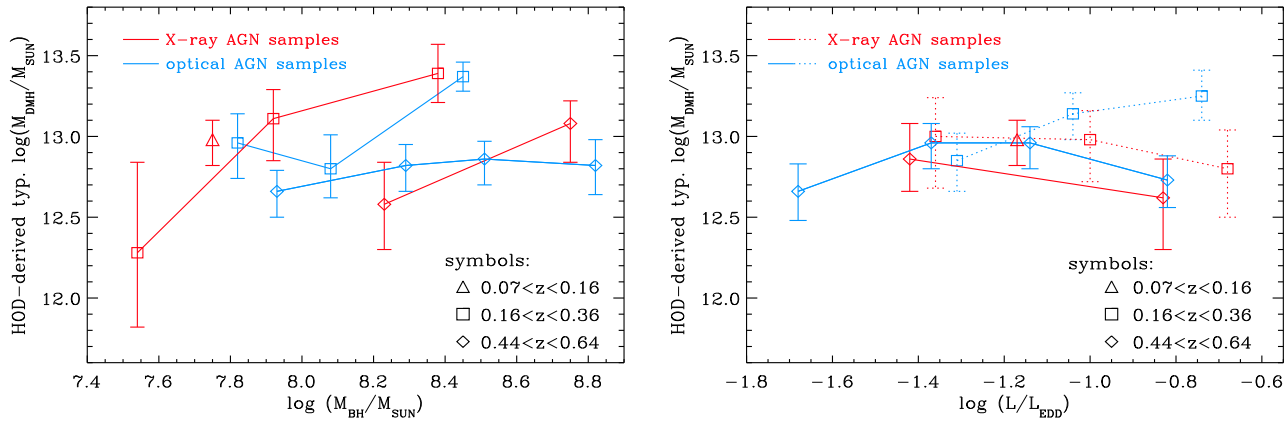

Figure 13. Left: typical DMH mass (derived from HOD modeling and grid fitting approach) as a function of $M_{\rm BH}$ at several independent redshifts (shown with different symbols) for X-ray (red symbols) and optical (blue symbols) AGN samples. Right: similar to the left panel, here as a function of the Eddington ratio. We show the results in the redshift range $0.16 < z < 0.36$ with dotted lines to allow for a clear distinction of the different samples.

correlation is found. Considering the relatively small uncertainties of the optical sample bias measurements, there is little room for even a weak clustering dependence with $M_{\rm i}$.

Shen et al. (2013) also explored the $M_{\rm i}$ clustering dependence of quasars using cross-correlation measurements between DR7 (optical) quasar catalog and Data Release 10 (DR10) CMASS galaxies. Their data are also consistent with no significant luminosity ($M_{\rm i}$) dependence. One difference is that they analyze a much wider redshift range from $0.3 < z < 0.9$, while we focus on a much narrower redshift range to exclude redshift evolution of the clustering properties as well as having better control of the systematics (e.g., constant stellar masses for CMASS galaxies). In addition, they also select their $M_{\rm i}$ subsamples differently. The advantage of these slightly different approaches, while finding the same (non)result, strengthens the robustness that there is no $M_{\rm i}$ clustering dependence for optical AGNs.

We also did not find an $M_{\rm i}$ clustering dependence in our previous work (Paper III) in the redshift ranges $0.16 < z < 0.36$ and $0.36 < z < 0.50$. In the lowest redshift range ($0.07 < z < 0.16$), we were not able to test for such a dependence due to the low number of objects. Thus, we conclude that from low to intermediate redshifts, there is no $M_{\rm i}$ clustering dependence for optically selected AGNs. This is in contrast to the result that in all of these redshift ranges we do find evidence for a weak $L_{\rm X}$ dependence in the X-ray-selected samples. In Paper IV, we gave as a possible explanation the complex sample selection for the optical SDSS sample (e.g., host galaxy/AGN separation). However, in the redshift range studied here, this effect should be minor. In the logical chain of correlations between $M_{\rm DMH} \rightarrow M_{\rm stellar} \rightarrow M_{\rm bulge} \rightarrow M_{\rm BH} \rightarrow M_{\rm i}$, there is a scatter at each stage, which sums across the chain. It is possible that the last step in the chain has a higher scatter than that of $M_{\rm BH} \rightarrow L_{\rm X}$, as for $L_{\rm X}$ we consistently detect a positive but weak clustering dependence and we find no dependence with $M_{\rm i}$. Another potential explanation is that there are different dependencies of $M_{\rm stellar}$–$L_{\rm X}$ (e.g., Carraro et al. 2022) and $M_{\rm stellar}$–$M_{\rm i}$.

6.5. M_{BH} Clustering Dependence and Its Evolution with Redshift

In the redshift range of $0.44 < z < 0.64$ studied here, we find only a tentative positive correlation of $M_{\rm BH}$ with the clustering strength for the X-ray AGN sample (1.3σ when comparing b values, 2.1σ confidence when comparing mean DMH masses). Despite the much larger sample size of the optical AGNs, the largest difference between the $M_{\rm BH}$ subsamples is only 1σ when comparing their bias values and 1.4σ when comparing mean DMH masses. This result is not sensitive to the specific cuts used in creating these subsamples or to reducing the number of subsamples (e.g., two subsamples only). Figure 6 (right) and Table 2 show that the X-ray and optical AGN samples span a similar parameter space in $M_{\rm BH}$. The samples differ only slightly in $L_{\rm H\beta}$ in that X-ray AGNs have on average higher $L_{\rm H\beta}$ than optical AGNs (Figure 6, left). Thus if a very weak $M_{\rm BH}$ dependence of the clustering strength exists, it remains unclear why the optical AGN samples do not reveal this correlation as the X-ray-selected AGN samples do.

In Figure 13 (left), we summarize the DMH mass dependence on $M_{\rm BH}$ measured in different redshift ranges for X-ray and optical BLAGN samples. At $0.07 < z < 0.16$, there are too few optical AGNs to compute a robust clustering signal. In this redshift range, there is a clear signal for X-ray AGNs; however, we are not able to create subsamples due to the relatively low number of objects. Thus in Figure 13 we show only the measurement for the total X-ray AGN sample in the redshift range $0.07 < z < 0.16$.

There is not a single $M_{\rm BH}$ versus DMH mass correlation across all redshifts, i.e., increasing $M_{\rm BH}$ does not necessarily result in higher DMH mass. Instead, we find that within each redshift range the DMH mass ranges are very similar across a range of $M_{\rm BH}$, consistent with a typical $M_{\rm DMH} \sim 10^{12.7-13.3}\,h^{-1}\,M_{\odot}$. For the redshift ranges in which $M_{\rm BH}$ subsamples can be created ($0.16 < z < 0.36$ and $0.44 < z < 0.64$), in both cases there is a weak positive correlation between $M_{\rm BH}$ and the typical DMH mass for X-ray-selected AGNs. For the optical AGN, no clear trend is found. Within a given redshift range, measurements between the X-ray and optical selections with similar $M_{\rm BH}$ agree well, within their uncertainties.

6.6. L/L_{EDD} Clustering Dependence and Evolution with Redshift

We do not find a correlation between $L/L_{\rm EDD}$ and typical DMH mass in the redshift range $0.44 < z < 0.64$; all subsamples, for both X-ray and optical AGNs, agree in the typical and mean DMH masses within their combined uncertainties at less than 1.3σ. In Figure 13 (right) we show the measurements for all redshift ranges. The results show that across all redshift

ranges studied, there is no clear clustering dependence with $L/L_{\rm EDD}$ and that at a given $L/L_{\rm EDD}$, the measurements from different redshifts agree well. Determining any $L/L_{\rm EDD}$ clustering dependence and its evolution with redshift for a hard X-ray-selected sample would provide a more complete picture than the current sample, as it would mitigate many observational biases (e.g., soft X-ray selection for our AGN sample).

6.7. L_{Bol} Clustering Dependence

We do not find a correlation between $L_{\rm Bol}$ and typical DMH mass in the redshift range $0.44 < z < 0.64$ for the two X-ray-selected AGN subsamples. However, in the same redshift range we find a $>2\sigma$ $L_{\rm Bol}$ dependence of the clustering strength in three of the four optical AGN subsamples. However, the highest $L_{\rm Bol}$ subsample (median log $(L_{\rm Bol}/[\rm erg\ s^{-1}]) = 45.67$) has almost identical clustering properties as the lowest $L_{\rm Bol}$ subsample (median log $(L_{\rm Bol}/[\rm erg\ s^{-1}]) = 44.80$). Although the X-ray-selected AGN sample has a smaller dynamic range in $L_{\rm Bol}$, there is overlap with the $L_{\rm Bol}$ range of the optically selected AGN sample. Within these individual subsamples we do not find a statistically significant discrepancy between the optical and X-ray-selected AGNs. As the $L_{\rm Bol}$ results taken together do not present a consistent picture of a clear dependence, we refrain from interpreting a possible trend to the data.

Unfortunately no observational constraints on the $L_{\rm Bol}$ dependence of AGN clustering exists from cross-correlation measurements at other redshifts. In the future, larger samples will be needed to more fully study the $L_{\rm Bol}$ clustering dependence at different redshifts.

7. Conclusions

In this paper, we extend our clustering studies of X-ray-selected (ROSAT/SDSS) and optically selected (SDSS) BLAGNs to the redshift range of $z = 0.44$–0.64. As in our previous work, we use a cross-correlation approach with a large set of tracer galaxies (here the CMASS galaxy sample) to substantially improve the S/N of the AGN clustering measurement. We define a CMASS galaxy sample to (i) have an identical average stellar mass (and thus clustering strength) over the entire redshift range used in this paper, and (ii) explore the AGN clustering properties down to scales of $r_p = 0.1\ h^{-1}$ Mpc. We estimate for the X-ray-selected and optically selected BLAGN samples the SMBH mass, accretion ratio relative to Eddington, and the bolometric luminosity based on spectral fits to the Hβ line. We split the AGN samples by the physical properties of luminosity in the selection bandpass, $M_{\rm BH}$, $L/L_{\rm EDD}$, and bolometric luminosity. We apply HOD modeling directly to the cross-correlation measurements to infer the AGN distribution as a function of DMH mass. We also determine the HOD parameters for the CMASS galaxy sample. For the full X-ray and optical AGN samples, we apply an MCMC HOD parameter search, while for the AGN subsamples, we apply a grid search to estimate the large-scale bias and typical and mean DMH mass of each sample.

The HOD constraints on the optical BLAGN sample are tighter than those for the X-ray BLAGN sample, due to a larger sample size. X-ray and optical BLAGNs have the same large-scale bias and thus extremely similar typical DMH masses (logarithmic DMH masses of $12.87^{+0.11}_{-0.19}\ h^{-1}M_{\odot}$ for the X-ray AGN sample and $12.72^{+0.06}_{-0.06}\ h^{-1}M_{\odot}$ for the optical AGN sample). While this reflects the typical DHM mass, the full range of halo masses occupied by AGNs is very broad (e.g., Georgakakis et al. 2019; Aird & Coil 2021). There is marginal statistical evidence that the one-halo clustering properties between the X-ray and optical AGN samples are different. In contrast to optically selected AGNs, X-ray-selected AGNs may have a larger population of satellite galaxies at $M_{\rm DMH} \sim 10^{13}\ h^{-1}\ M_{\odot}$, indicated by the higher satellite fraction and lower $\alpha_{\rm s}$ (satellite slope) found for the X-ray AGN HOD compared to the optical AGN HOD.

When we compare results as a function of AGN properties, we do not find statistically significant correlations with $L/L_{\rm EDD}$ and M_i. For the X-ray-selected AGN sample, we find a positive correlation between mean DMH mass and $L_{\rm X}$ as well as with $M_{\rm BH}$ at a $>2\sigma$ confidence level. The optical AGN sample does not show a significant correlation between mean DMH mass and $M_{\rm BH}$, but the measured values for the different optical subsamples also do not contradict the $M_{\rm BH}$ versus mean and typical DMH mass correlations found for the X-ray-selected AGN sample. Within the optical BLAGN sample, we find some dependencies at $>2\sigma$ confidence level in the clustering properties as a function of $L_{\rm Bol}$. However, the lowest $L_{\rm Bol}$ and highest $L_{\rm Bol}$ samples have very similar clustering properties, so a clear trend is not present.

We compare our results with those obtained in Paper III, in which we evaluate the clustering and HOD properties of X-ray (RASS/SDSS) and optically selected (SDSS) BLAGNs in three lower-redshift ranges using different SDSS galaxy tracer sets. The full redshift range of $z = 0.07$–0.64 covered by all of these studies spans a cosmic time interval of 5 Gyr. In all redshift ranges, we use the same cross-correlation technique to determine the AGN clustering properties, create samples from the same large area surveys (RASS and SDSS), and evaluate the results with similar HOD modeling. We find that X-ray and optically selected BLAGNs, despite their different optical and X-ray luminosities at different redshifts, occupy DMHs with $M^{\rm typ}_{\rm DMH} \sim 10^{12.5-13.0}\ h^{-1}\ M_{\odot}$ across this full redshift range. In other words, we find no statistically significant difference in the typical DMH masses between X-ray and optically selected BLAGN samples. However, at higher redshift, the same DMH mass hosts more X-ray luminous AGNs than at lower redshift.

Semianalytic cosmological simulations find that an $L_{\rm X}$ and $M_{\rm BH}$ dependence of the AGN clustering exists, but only for the most-luminous AGNs and not for low- or moderate-luminosity AGNs. Since our X-ray-selected BLAGN sample contains the most-luminous objects in independent redshift bins, we can test this prediction. From $z = 0.07$ to $z = 0.64$, we also find weak positive correlations between the typical DMH mass and $L_{\rm X}$ for the X-ray BLAGN samples. In the redshift ranges $z = 0.16$–0.36 and $z = 0.44$–0.64, we can estimate $M_{\rm BH}$, and we have enough objects to create subsamples in $M_{\rm BH}$ and $L/L_{\rm EDD}$. We find that the weak positive $L_{\rm X}$ dependence of the AGN clustering appears to be due to a weak positive $M_{\rm BH}$ dependence of the clustering signal, in that more X-ray luminous (and larger $M_{\rm BH}$) BLAGNs reside in more-massive DMHs than their lower X-ray luminosity (lower $M_{\rm BH}$) counterparts. The observed clustering strength across the full redshift range does not depend on $L/L_{\rm EDD}$. Consequently, higher accretion rate AGNs do not reside in more dense environments.

The number of RASS-detected AGNs decreases sharply below $z \lesssim 0.07$ and above $z \gtrsim 0.6$, due to limited volumes at low redshift and ROSAT's flux sensitivity. Consequently, the redshift range for high-S/N clustering studies using RASS-selected AGNs cannot be extended further. However, the X-ray telescope eROSITA (Predehl et al. 2021) is a game changer for AGN studies. eROSITA is far more sensitive than ROSAT and scans the entire sky several times at X-ray wavelengths. The resulting stacked X-ray data will reach a flux limit ∼30 times more sensitive than RASS. This will provide unprecedented large AGN samples for clustering studies to improve constraints on dependences with redshift, L_X, and M_{BH}, as well as to test if the one-halo properties of X-ray and optically selected AGNs differ. Recently the German eROSITA team published its first AGN clustering paper (Comparat et al. 2023) using several thousand AGNs detected in the ∼140 square degree eROSITA Final Equatorial Depth Survey field (Brunner et al. 2022; Liu et al. 2022). The spectroscopic AGN samples from the eROSITA all-sky survey scans will contain hundreds of thousands of objects and will thus bring AGN clustering studies to a new level.

Acknowledgments

The research leading to these results has received funding from the European Community's Seventh Framework Programme (/FP7/2007-2013/) under grant agreement No. 229517.

M.K. acknowledges support by DFG grant Nos. KR 3338/3-1 and KR 3338/4-1. T.M. and H.A. acknowledge support from UNAM-DGAPA (PAPIIT IN111319, IN114423, and PASPA) and CONACyT (grant Científica Básica 252531). T.M. thanks Leibniz-Institut für Astrophysik Potsdam (AIP) for hospitality during his sabbatical leave from UNAM. A.L.C. acknowledges support from the Ingrid and Joseph W. Hibben Chair at UC San Diego. We thank Xan Morice-Atkinson for his support on the photometric redshift estimates. The ROSAT Project was supported by the Bundesministerium für Bildung und Forschung (BMBF/DLR) and the Max-Planck-Gesellschaft (MPG).

Funding for the Sloan Digital Sky Survey IV has been provided by the Alfred P. Sloan Foundation, the U.S. Department of Energy Office of Science, and the Participating Institutions. SDSS acknowledges support and resources from the Center for High-Performance Computing at the University of Utah. The SDSS website is www.sdss.org.

SDSS is managed by the Astrophysical Research Consortium for the Participating Institutions of the SDSS Collaboration including the Brazilian Participation Group, the Carnegie Institution for Science, Carnegie Mellon University, Center for Astrophysics/Harvard and Smithsonian (CfA), the Chilean Participation Group, the French Participation Group, Instituto de Astrofísica de Canarias, The Johns Hopkins University, Kavli Institute for the Physics and Mathematics of the universe (IPMU) / University of Tokyo, the Korean Participation Group, Lawrence Berkeley National Laboratory, Leibniz-Institut für Astrophysik Potsdam (AIP), Max-Planck-Institut für Astronomie (MPIA Heidelberg), Max-Planck-Institut für Astrophysik (MPA Garching), Max-Planck-Institut für Extraterrestrische Physik (MPE), National Astronomical Observatories of China, New Mexico State University, New York University, University of Notre Dame, Observatório Nacional / MCTI, The Ohio State University, Pennsylvania State University, Shanghai Astronomical Observatory, United Kingdom Participation Group, Universidad Nacional Autónoma de México, University of Arizona, University of Colorado Boulder, University of Oxford, University of Portsmouth, University of Utah, University of Virginia, University of Washington, University of Wisconsin, Vanderbilt University, and Yale University.

Appendix A
Recovering the Small-scale Clustering Signal

The full CMASS sample is designed to facilitate the primary science goal of detection of the baryon acoustic oscillation signal at $z \sim 0.6$ (Cuesta et al. 2016). Since two fibers cannot be placed closer than 62″ for approximately 5.5% of all photometrically selected CMASS candidates, no optical spectrum could be obtained for these sources (Guo et al. 2013). This strongly affects small-scale clustering measurements. The CMASS survey accounts for these restrictions by introducing weights to observed galaxies (Reid et al. 2016; Ross et al. 2020). If a spectroscopically observed CMASS galaxy has, e.g., two close neighbors that fulfill the CMASS selection criteria but are spectroscopically missed due to fiber collisions, the CMASS galaxy that was observed is given a weight of three, to account for the two missing galaxies. Other observational biases are also considered and folded into the weights. These weights ensure that large-scale galaxy-galaxy pair counts are correctly recovered. The total weight for each object is calculated by $w_{tot} = (w_{CP} + w_{NOZ} - 1) \times w_{sys}$, where w_{CP} is the weight based on fiber-collision pairs, w_{NOZ} accounts for spectroscopic objects for which no redshift information could be obtained, and w_{sys} accounts for systematic effects due to the varying star density across the SDSS footprint, which affects the observed density of galaxies. More details on the weights can be found in Ross et al. (2012) and Anderson et al. (2012).

While such weighting recovers missed galaxy pair counts on large scales, this approach does not allow us to correctly recover the correlation function on scales less than $\sim 0.5\ h^{-1}$ Mpc (corresponding to 62″ at $z = 0.55$, the median redshift of our sample), as shown in Figure 14 (left). On these small scales, it is necessary to either use information from the photometric catalogs about pairs of galaxies that could not both be spectroscopically observed, or other correction methods developed in the literature. To recover the CMASS small-scale clustering signal, different approaches have been used (e.g., Guo et al. 2013; Mohammad et al. 2020). Guo et al. (2013) presented a method that divides the CMASS sample into two distinct populations. The first is drawn from SDSS regions covered by multiple masks where fiber collisions are minimized. The second population originates from SDSS regions that are affected by fiber collisions because they are only observed by one mask. The clustering signal on small scales can be estimated using the first population only, within the overlapping regions, and on larger scales is measured using the full SDSS footprint. Recently, Mohammad et al. (2020) introduced a "pairwise-inverse probability and angular upweighting" method for this correction, which recovers clustering measurements down to $\sim 0.1\ h^{-1}$ Mpc scales. As shown below, our alternative approach, which is developed independently and explained in the rest of this subsection, also allows us to correct for the fiber collision at similar small scales.

To begin, we use the DR12 target catalog, which is based solely on SDSS photometric data. Using the different selection criteria, e.g., color cuts, this catalog contains information on which photometric objects should receive a fiber and why this target was selected (i.e., which object class). As described above, not all of these targets can be spectroscopically

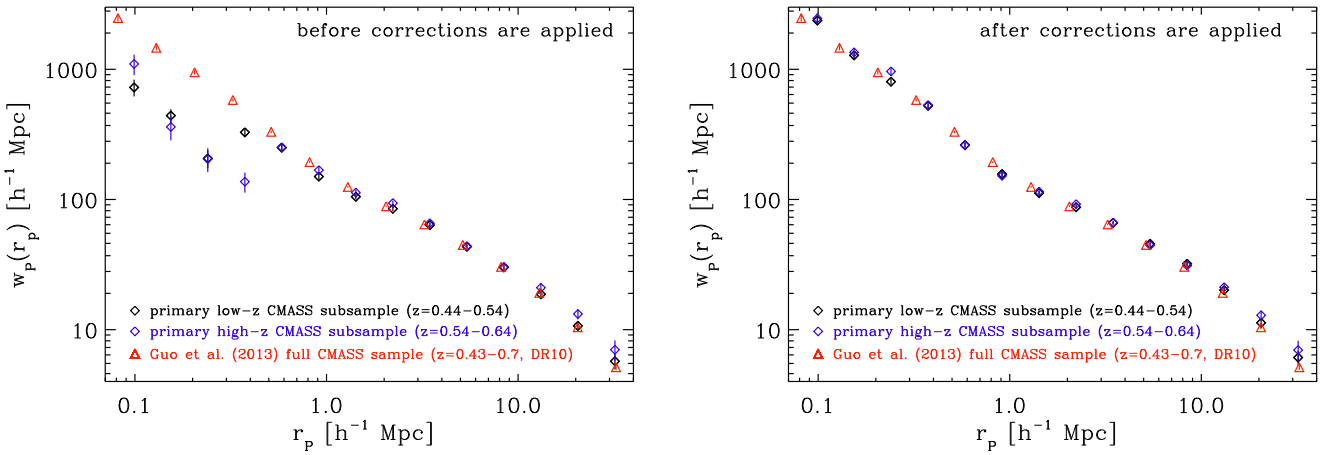

Figure 14. Left: comparison between the ACFs of a CMASS sample with $0.44 < z < 0.64$ and $11.25 < \log(M_{\rm stellar}/M_{\odot}) < 11.43$ when split into low- and high-redshift subsamples, *before* applying our correction algorithm. In addition we show the full Guo et al. (2013) CMASS sample, which utilizes a different approach to correct the small-scale clustering. Right: similar to the left panel showing the low- and high-redshift CMASS subsamples, here *after* our correction algorithm is applied.

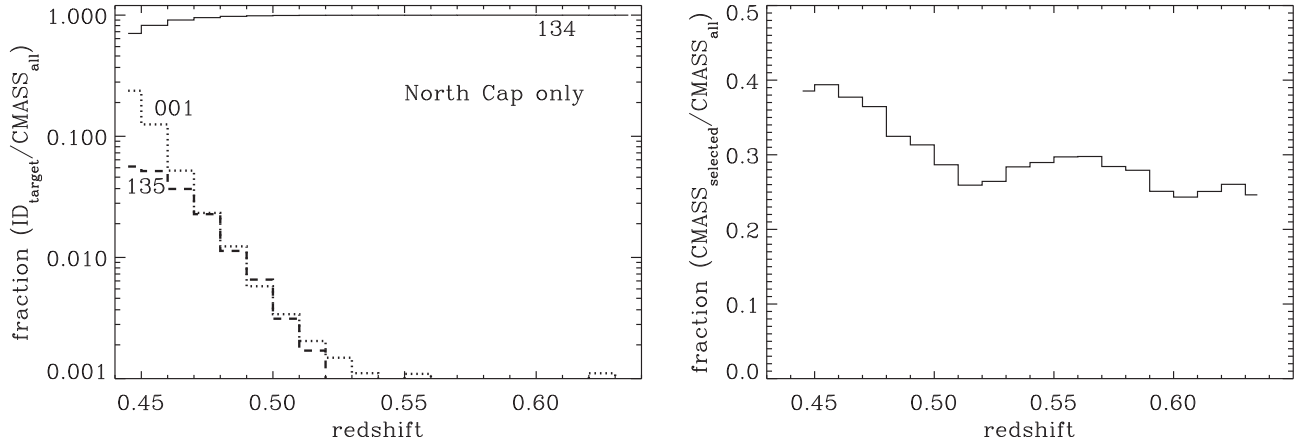

Figure 15. Left: fraction of different target IDs (bitmask values) to the full spectroscopic CMASS sample as a function of redshift (SDSS North Cap). Each line represents a different target ID whose tag is stated directly next to the corresponding line. Right: fraction of spectroscopic CMASS sources that fulfill our final selection criteria to the full spectroscopic CMASS sample as a function of redshift.

observed due to fiber collisions. The target catalog encodes information about why an object was targeted for spectroscopic follow-up observation using target IDs.[16] These targets IDs are bitmask values. We identify all photometric target IDs in the North Cap that lead to spectroscopically confirmed CMASS objects. Of those, we consider only IDs that lead to at least 100 spectroscopically confirmed CMASS galaxies. For the resulting target IDs (001, 134, 135), we compute the fraction c of spectroscopic CMASS targets with each of these IDs over photometric targets with these IDs ($c_{001} = 0.253$, $c_{134} = 0.872$, $c_{135} = 0.008$). The meaning of these number is, e.g., that 25.3% of photometric targets with ID 001 led to spectroscopically confirmed CMASS objects.

Then we calculate the redshift distribution ($f_{\rm ID\_target}(z)$) of spectroscopic CMASS galaxies with these IDs in the range $0.44 < z < 0.64$ (bin size $\Delta z = 0.01$). Figure 15 (left) shows that spectroscopic CMASS galaxies with ID 134 are by far the dominant population. In each redshift bin, the sum over all three target IDs is 1. Thus this provides the normalized relative contribution of each target ID as a function of redshift.

[16] http://www.sdss3.org/dr10/algorithms/bitmask_boss_target1.php

Next we determine from Figure 1 the fraction $f_{\rm selected/all}(z)$ of spectroscopic CMASS objects that fulfill our final selection criteria of $0.44 \leqslant z \leqslant 0.64$ and stellar mass selection (red data points) relative to the full spectroscopic CMASS sample (red +black data points) as a function of redshift. The result is shown in Figure 15 (right). With this information in hand, we are able to perform a statistical correction for the fiber collisions based on the photometric target catalog. To recover the small-scale clustering signal, we compute, for each photometric galaxy that has a fiber collision with a spectroscopic CMASS object, the probability that the photometric source (based on its photometric target ID and the redshift) should be assigned the redshift of the spectroscopic CMASS object and include it in the final sample as follows:

$$P(ID, z) = c_{\rm ID-target} \times f_{\rm ID-target}(z) \times f_{\rm selected/all}(z) - P_{\rm spur}. \quad \text{(B1)}$$

In practice, we search for all photometric targets that have IDs with the values 001, 134, or 135 within a radius of 62″ of each selected spectroscopic CMASS galaxy. Photometric targets within the search radius that already have spectroscopic data are rejected. If the spectroscopic CMASS galaxy has $w_{\rm CP} > 1$,

we use the redshift of the spectroscopic CMASS object that the object collides with and calculate the probability $P(ID, z)$ according Equation (B1). We then draw a random value $n_{\rm random}$ between 0 and 1 for each colliding target. If $n_{\rm random} \leqslant P(ID, z)$, we consider this object for our collision correction further; otherwise, we reject it. The term $P_{\rm spur}$ corrects for spurious matches. The number density per sky area for the photometric targets with the CMASS IDs is 8.78×10^{-6} arcsec^{-2}. We calculate the distance between the spectroscopically confirmed CMASS object and the collided object. Using a simple circular area calculation (distance = radius) and considering the number density provides the chance that the collided object will spuriously fall at its observed position.

If $n_{\rm random} \leqslant P(ID, z)$, we adopt the R.A. and decl. of the photometric object and assign it the same redshift as the nearby spectroscopic CMASS galaxy. Finally, we recompute $w_{\rm CP}$ for the spectroscopic CMASS galaxy by $w_{\rm CP,NEW} = w_{\rm CP,OLD} - 1$ if the collided object ends up being in our sample. This approach is repeated for the same spectroscopic CMASS galaxy if it collides with more than one object until $w_{\rm CP} > 1$ is not fulfilled anymore. If more than one object collides with a spectroscopic CMASS galaxy, we sort all objects by distance from the spectroscopic object and start by calculating (thus potentially correcting) the closest photometric object first. This approach accounts for the fact that close neighbors have a substantially higher probability of having similar redshifts.

Our approach for correcting the fiber-collision issue in the CMASS sample has several advantages: (i) it does not affect the large-scale clustering above $\sim$0.5 h^{-1} Mpc, because for each collision-corrected object we include in our final sample, we reduce the weight ($w_{\rm CP}$) by 1, (ii) the resulting clustering signal is very similar in shape and amplitude to that measured for the full CMASS sample from SDSS DR10 by Guo et al. (2013; $0.43 < z < 0.7$), and most importantly for our cross-correlation method (iii) when split into lower- and higher-redshift subsamples ($0.44 < z < 0.54$ and $0.54 < z < 0.64$, respectively), the clustering signal has minimal differences, well within the expected statistical uncertainties (Figure 14, right). We additionally tested various approaches using photometric redshifts to correct the small-scale clustering signal. However, these approaches resulted in strong discrepancies between the low- and high-redshift CMASS samples at small scales.

Appendix B
Reliability of the Hβ Broad-line Fit

In order to assess the reliability of our broad-line fits, we carry out Monte Carlo simulations using 21 objects in the X-ray catalog with S/N >50, stepwise degrading their S/N by adding random Gaussian noise, fitting the degraded spectra with our fitting routine, and measuring the FWHM from the best fit to the degraded spectrum. For each AGN, we perform 100 simulations per S/N bin. Following Paper IV, we require an uncertainty on the Hβ FWHM measurement of <40%, as above that value the uncertainties exceed the commonly assumed systematic uncertainties for viral $M_{\rm BH}$ estimates of $\sim$0.3 dex. As shown in the upper panel in Figure 16 at S/N = 5, roughly 90% of our targets fulfill this requirement on the recovered FWHM. We therefore use S/N = 5 as our default threshold for spectra for which we determine $M_{\rm BH}$, and we verify that our results do not depend on the precise S/N value chosen. Our results agree with previous work, suggesting that at an S/N below $\sim$5, the uncertainties on FWHM dominate the $M_{\rm BH}$ measurement (e.g., Denney et al. 2009; Shen et al. 2011). The typical FWHM uncertainty at S/N = 5 is $\sim$0.06 dex, as shown in the bottom panel of Figure 16. After applying the S/N >5 threshold, we have a sample size of 1632 for the X-ray AGN sample and 8889 for the optical AGN sample.

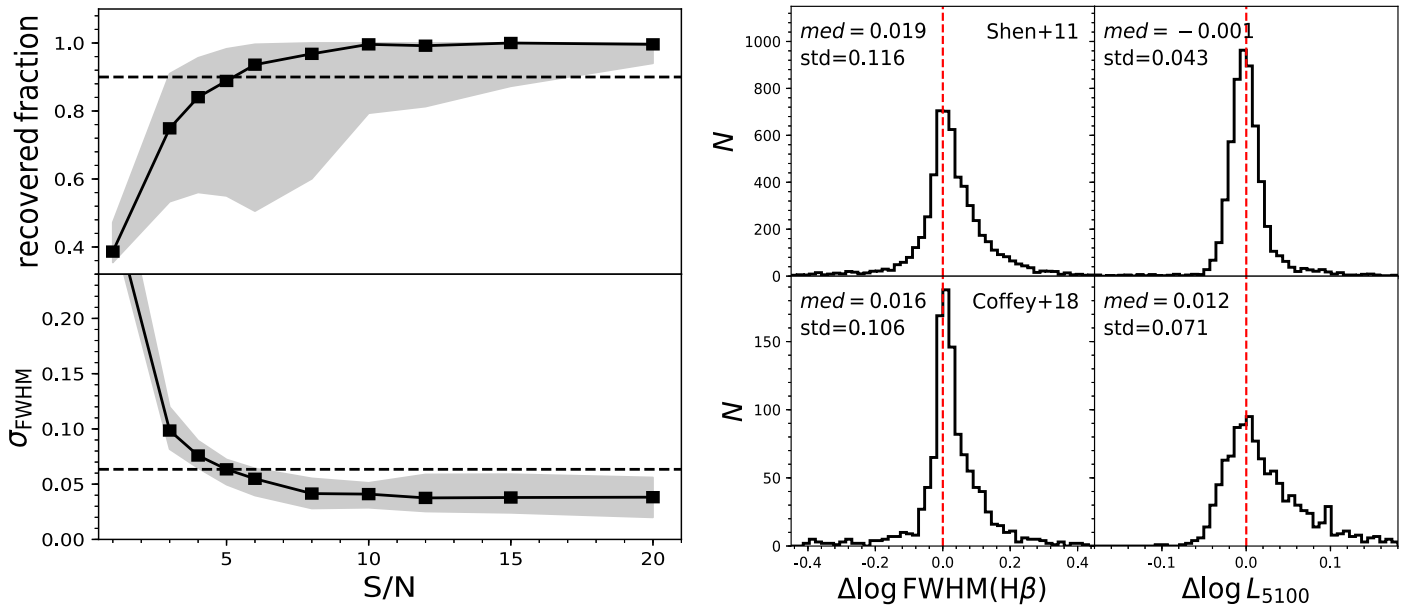

Figure 16. Upper-left: simulation of the recovery rate of the intrinsic FWHM of Hβ within a 40% uncertainty as a function of spectral S/N, based on Monte Carlo simulations for 21 AGN spectra. Lower-left: dependence of the mean uncertainty on the FWHM measurement as a function of S/N. The gray areas show the 68% (1σ) uncertainty range based on the simulated spectra with degraded S/N properties. Right: comparison of the FWHM (left panels) and L_{5100} measurements (right panels) between our samples and those from the literature. Upper-right: comparison between our optical DR14 AGN catalog and the SDSS DR7 quasar catalog by Shen et al. (2011). Lower-right: comparison of our X-ray sample with the SDSS/SPIDERS (2RXS) catalog by Coffey et al. (2019).

Appendix C
Comparing our Hβ Fit Results to Literature Measurements

Our sample overlaps with previous studies of the spectral properties of AGNs in the SDSS. We compare our Hβ measurements with other studies, to investigate the consistency of our results with previous work. In particular we cross-match our optical AGN sample (DR14) with the SDSS DR7 quasar catalog of Shen et al. (2011) and our SPIDERS X-ray-selected AGN sample with the recent study by Coffey et al. (2019). The SDSS DR7 quasar catalog is a subset of the DR14 quasar catalog by Pâris et al. (2018) with 5764 objects in common with our optical DR14 sample. In the upper panels of Figure 16, we compare the FWHM and L_{5100} measurements of Shen et al. (2011) to ours. We find an excellent agreement overall, with median differences in $\log\mathrm{FWHM} = 0.02$ and $\log L_{5100} = 0.00$ and a standard deviation of 0.12 dex and 0.04 dex, respectively. Coffey et al. (2019) presented an M_{BH} catalog for SPIDER AGNs from the 2RXS catalog with 1124 AGNs in common with our X-ray sample. We show this comparison in the lower panels of Figure 16. For the FWHM measurement, we find a similar agreement as in the comparison with Shen et al. (2011), providing an estimate of the systematic uncertainties of the line width measurements. For the continuum luminosity, L_{5100}, we find a consistent mode, but there is a tail with lower L_{5100} in the Coffey et al. (2019) catalog. This is caused by the inclusion of a host galaxy template in the fitting procedure of the continuum in Coffey et al. (2019). We do not explicitly account for the host galaxy contribution in our fitting routine, since for our sample it is often difficult to break the degeneracy between host galaxy spectrum and AGN continuum emission. We account for the effect of host galaxy contamination to L_{5100} in a statistical fashion, as detailed in Section 3.2.

The differences between our method and those of Shen et al. (2011) and Coffey et al. (2019) lead to uncertainties in the M_{BH} estimates that are lower than the systematic uncertainties of ∼0.3 dex; thus, we conclude that our line fitting routine provides robust measurements of the Hβ region spectral properties and enables the estimation of black hole masses based on these measurements.

ORCID iDs

Takamitsu Miyaji https://orcid.org/0000-0002-7562-485X
Andreas Schulze https://orcid.org/0000-0002-6660-6131
Alison L. Coil https://orcid.org/0000-0002-2583-5894
Johan Comparat https://orcid.org/0000-0001-9200-1497
Mara Salvato https://orcid.org/0000-0001-7116-9303
Andrea Merloni https://orcid.org/0000-0002-0761-0130
Kirpal Nandra https://orcid.org/0000-0002-7150-9192
Joel R. Brownstein https://orcid.org/0000-0002-8725-1069
Donald P. Schneider https://orcid.org/0000-0001-7240-7449

References

Abolfathi, B., Aguado, D. S., Aguilar, G., et al. 2018, ApJS, 235, 42
Adelman-McCarthy, J., Agüeros, M. A., Allam, S. S., et al. 2006, ApJS, 162, 38
Aird, J., & Coil, A. L. 2021, MNRAS, 502, 5962
Alam, S., Albareti, F. D., Allende Prieto, C., et al. 2015, ApJS, 219, 12
Allevato, V., Finoguenov, A., Cappelluti, N., et al. 2011, ApJ, 736, 99
Altamirano-Dévora, L., Miyaji, T., Aceves, H., et al. 2016, RMxAA, 52, 11
Anderson, L., Aubourg, E., Bailey, S., et al. 2012, MNRAS, 427, 3435
Bentz, M. C., et al. 2009, ApJ, 697, 160
Blanton, M. R., Bershady, M. A., Abolfathi, B., et al. 2017, AJ, 154, 28
Boller, Th, Freyberg, M. J., Trümper, J., et al. 2016, A&A, 588, 103
Bolton, A. S., Schlegel, D. J., Aubourg, É., et al. 2012, AJ, 144, 144
Booth, C. M., & Schaye, J. 2010, MNRAS, 405, L1
Boroson, T. A., & Green, R. F. 1992, ApJS, 80, 109
Brunner, H., Liu, T., Lamer, G., et al. 2022, A&A, 661, 1
Cappelluti, N., Ajello, M., Burlon, D., et al. 2010, ApJL, 716, L209
Cardelli, J. A., Clayton, G. C., & Mathis, J. S. 1989, ApJ, 345, 245
Carraro, R., Shankar, F., Viola, A., et al. 2022, MNRAS, 512, 1185
Coffey, D., Salvato, M., Merloni, M., et al. 2019, A&A, 625, 123
Coil, A. L., Georgakakis, A., Newman, J. A., et al. 2009, ApJ, 701, 1484
Coil, A. L., Hennawi, J. F., Newman, J., et al. 2007, ApJ, 654, 115
Comparat, J., Luo, W., Merloni, A., et al. 2023, A&A, 673, A122
Comparat, J., Maraston, C., Goddard, D., et al. 2017, arXiv:1711.06575
Comparat, J., Merloni, A., Dwelly, T., et al. 2020, A&A, 636, 22
Comparat, J., Merloni, A., Salvato, M., et al. 2019, MNRAS, 487, 2005
Cooray, A., & Sheth, R. 2002, PhR, 372, 1
Cuesta, A. J., Vargas-Magnana, M., Beutler, F., et al. 2016, MNRAS, 457, 1770
Davis, M., & Peebles, P. J. E. 1983, ApJ, 267, 465
Dawson, K. S., Schlegel, D. J., Ahn, C. P., et al. 2013, AJ, 145, 10
Denney, K. D., Peterson, B. M., Dietrich, M., Vestergaard, M., & Bentz, M. C. 2009, ApJ, 692, 246
Eftekharzadeh, S., Myers, A. D., White, M., et al. 2015, MNRAS, 453, 2779
Eisenstein, D. J., Weinberg, D. H., Agol, E., et al. 2011, AJ, 142, 72
Fakhouri, O., Ma, C.-P., & Boylan-Kolchin, M. 2010, MNRAS, 406, 2267
Georgakakis, A., Comparat, J., Merloni, A., et al. 2019, MNRAS, 487, 275
Gilli, R., Daddi, E., Zamorani, G., et al. 2005, A&A, 430, 811
Gilli, R., Zamorani, G., Miyaji, T., et al. 2009, A&A, 494, 33
Gunn, J. E., Siegmund, W. A., Mannery, E. J., et al. 2006, AJ, 131, 2332
Guo, H., Zehavi, I., Zheng, Z., et al. 2013, ApJ, 767, 122
Guo, H., Zheng, Z., Zehavi, I., et al. 2015, MNRAS, 446, 578
Hasinger, G., Miyaji, T., & Schmidt, M. 2005, A&A, 441, 417
Kaiser, N. 1987, MNRAS, 227, 1
Kaspi, S., Smith, P. S., Netzer, H., et al. 2000, ApJ, 533, 631
Kelly, B. C., & Shen, Y. 2013, ApJ, 764, 45
Koutoulidis, L., Plionis, M., Georgantopoulos, I., & Fanidakis, N. 2013, MNRAS, 428, 1382
Krishnan, C., Almaini, O., Hatch, N. A., et al. 2020, MNRAS, 494, 1693
Krumpe, M., Miyaji, T., & Coil, A. L. 2010, ApJ, 713, 558, (Paper I)
Krumpe, M., Miyaji, T., & Coil, A. L. 2014, in Acta Polytech. Proc. 1, Multifrequency Behaviour of High Energy Cosmic Sources, ed. F. Giovannelli & L. Sabau-Graziati (Prague: CTU), 71
Krumpe, M., Miyaji, T., Coil, A. L., & Aceves, H. 2012, ApJ, 746, 1, (Paper III)
Krumpe, M., Miyaji, T., Coil, A. L., & Aceves, H. 2018, MNRAS, 474, 1773
Krumpe, M., Miyaji, T., Husemann, B., et al. 2015, ApJ, 815, 21, (Paper IV)
Landy, S. D., & Szalay, A. S. 1993, ApJ, 412, 64
Larson, D., Dunkley, J., Hinshaw, G., et al. 2011, ApJS, 192, 16
Laurent, P., Eftekharzadeh, S., Le Goff, J.-M., et al. 2017, JCAP, 07, 017
Law-Smith, J., & Eisenstein, D. J. 2017, ApJ, 836, 87
Leauthaud, A., Benson, A., Civano, F., et al. 2015, MNRAS, 446, 1874
Leauthaud, A., Bundy, K., Saito, S., et al. 2016, MNRAS, 457, 4021
Liu, T., Buchner, J., Nandra, K., et al. 2022, A&A, 661, 5
Makino, J., & Hut, P. 1997, ApJ, 481, 83
Maraston, C., Pforr, J., Henriques, B. M., et al. 2013, MNRAS, 435, 2764
Maraston, C., & Strömbäck, G. 2011, MNRAS, 418, 2785
Marconi, A., Risaliti, G., Gilli, R., et al. 2004, MNRAS, 351, 169
Markwardt, C. B. 2009, in ASP Conf. Ser. 411, Astronomical Data Analysis Software and Systems XVIII, ed. D. A. Bohlender, D. Durand, & P. Dowler (San Francisco, CA: ASP), 251
McLure, R. J., & Dunlop, J. S. 2004, MNRAS, 352, 1390
McLure, R. J., & Jarvis, M. J. 2002, MNRAS, 337, 109
Mejía-Restrepo, J. E., Trakhtenbrot, B., Lira, P., Netzer, H., & Capellupo, D. M. 2016, MNRAS, 460, 187
Melnyk, O., Elyiv, A., Smolcic, V., et al. 2018, A&A, 620, A6
Mendez, A. J., Coil, A. L, Aird, J., et al. 2016, ApJ, 821, 55
Meneux, B., Guzzo, L., de la Torre, S., et al. 2009, A&A, 505, 463
Miyaji, T., Hasinger, G., & Schmidt, M. 2001, A&A, 369, 49
Miyaji, T., Krumpe, M., Coil, A. L., & Aceves, H. 2011, ApJ, 726, 83, (Paper II)
Mohammad, F. G., Percival, W. J., Seo, H.-J., et al. 2020, MNRAS, 498, 128
Mountrichas, G., & Georgakakis, A. 2012, MNRAS, 420, 514

Mountrichas, G., Georgakakis, A., & Georgantopoulos, I. 2019, MNRAS, 483, 1374
Mullaney, J. R., Alexander, D. M., Fine, S., et al. 2013, MNRAS, 433, 622
Myers, A. D., Palanque-Delabrouille, N., Prakash, A., et al. 2015, ApJS, 221, 27
Navarro, J. F., Frenk, C. S., & White, S. D. M. 1997, ApJ, 490, 493
Netzer, H., & Trakhtenbrot, B. 2007, ApJ, 654, 754
Nuza, S., Sánchez, A. G., Prada, F., et al. 2013, MNRAS, 432, 743
Pâris, J., Petitjean, P., Aubourg, E., et al. 2018, A&A, 613, 51
Peebles, P. J. E. 1980, The Large-Scale Structure of the Universe (Princeton, NJ: Princeton Univ. Press)
Peterson, B. M., & Wandel, A. 2000, ApJL, 540, L13
Plionis, M., Koutoulidis, L., Koulouridis, E., et al. 2018, A&A, 620, A17
Porciani, C., Magliocchetti, M., & Norberg, P. 2004, MNRAS, 355, 1010
Powell, M. C., Cappelluti, N., Urry, C. M., et al. 2018, ApJ, 858, 110
Powell, M. C., Urry, C. M., Cappelluti, N., et al. 2020, ApJ, 891, 41
Predehl, P., Andritschke, R., Arefiev, V., et al. 2021, A&A, 647, 1
Prugniel, P., Soubiran, C., Koleva, M., & Le Borgne, D. 2007, arXiv: astro-ph/0703658
Reid, B., Ho, S., Padmanabhan, N., et al. 2016, MNRAS, 455, 1553
Richards, G. T., Strauss, M. A., Fan, X., et al. 2006, AJ, 131, 2766
Rodríguez-Torres, S. A., Chuang, C.-H. J., & Prada, F. 2016, MNRAS, 460, 1173
Rodríguez-Torres, S. A., Comparat, J., Prada, F., et al. 2017, MNRAS, 468, 728
Ross, A. J., Bautista, J., Tojeiro, R., et al. 2020, MNRAS, 498, 2354
Ross, A. J., Beutler, F., Chuang, C.-H., et al. 2017, MNRAS, 464, 1168
Ross, A. J., Percival, W. J., Sanchez, A. G., et al. 2012, MNRAS, 424, 564
Ross, N. P., Shen, Y., Strauss, M. A., et al. 2009, ApJ, 697, 1634
Salpeter, E. E. 1955, ApJ, 121, 161
Salvato, M., Buchner, J., Budavári, T., et al. 2018, MNRAS, 473, 4937
Savitzky, A., & Golay, M. J. E. 1964, AnaCh, 36, 1627
Schlegel, D. J., Finkbeiner, D. P., & Davis, M. 1998, ApJ, 500, 525
Schulze, A., Bongiorno, A., Gavignaud, I., et al. 2015, MNRAS, 447, 2085
Schulze, A., Schramm, M., Zuo, W., et al. 2017, ApJ, 848, 104
Schulze, A., Silverman, J. D., Kashino, D., et al. 2018, ApJS, 239, 22
Shankar, F., Allevato, V., Bernardi, M., et al. 2020, NatAs, 4, 282
Shen, Y., McBride, C. K., White, M., et al. 2013, ApJ, 778, 98
Shen, Y., Richards, G. T., Strauss, M. A., et al. 2011, ApJS, 194, 45
Sheth, R. K., Mo, H. J., & Tormen, G. 2001, MNRAS, 323, 1
Smee, S. A., Gunn, J. E., Uomoto, A., et al. 2013, AJ, 146, 32
Springel, V. 2005, MNRAS, 364, 1105
Sunyaev, R., Arefiev, V., Babyshkin, V., et al. 2021, A&A, 656, A132
Tinker, J. L., Weinberg, D. H., Zheng, Z., & Zehavi, I. 2005, ApJ, 631, 41
Trakhtenbrot, B., & Netzer, H. 2012, MNRAS, 427, 3081
Trümper, J. 1982, AdSpR, 2, 241
van den Bosch, F. C., More, S., Cacciato, M., Mo, H., & Yang, X. 2013, MNRAS, 430, 725
Vestergaard, M., & Peterson, B. M. 2006, ApJ, 641, 689
Viitanen, A., Allevato, V., Finoguenov, A., et al. 2019, A&A, 629, A14
Voges, W., Aschenbach, B., Boller, T., et al. 1999, A&A, 349, 389
Voges, W., Aschenbach, B., Boller, T., et al. 2000, yCat, 9029, 0
White, M., Blanton, M., Bolton, A., et al. 2011, ApJ, 728, 126
White, S. D. M., & Frenk, C. S. 1991, ApJ, 379, 52
Wilkinson, D. M., Maraston, C., Goddard, D., Thomas, D., & Parikh, T. 2017, MNRAS, 472, 4297
Yang, Y., Mushotzky, R. F., Barger, A. J., & Cowie, L. L. 2006, ApJ, 645, 68
Zehavi, I., Zheng, Z., Weinberg, D. H., et al. 2011, ApJ, 736, 59
Zheng, Z., Coil, A., & Zehavi, I. 2007, ApJ, 667, 760
Zheng, Z., Zehavi, I., Eisenstein, D. J., Weinberg, D. H., & Jing, Y. P. 2009, ApJ, 707, 554